# SANDIA REPORT

SAND2006-6577
Unlimited Release
Printed October 2006

# A Tunable Electrochromic Fabry-Perot Filter for Adaptive Optics Applications

Daniel R. Kammler, William G. Yelton, Jason C. Verley, Edwin J. Heller, Jonathan D. Blaich, William C. Sweatt, and Andrea Ambrosini

Prepared by
Sandia National Laboratories
Albuquerque, New Mexico 87185 and Livermore, California 94550

Sandia is a multiprogram laboratory operated by Sandia Corporation,
a Lockheed Martin Company, for the United States Department of Energy's
National Nuclear Security Administration under Contract DE-AC04-94AL85000.

Sandia National Laboratories

Issued by Sandia National Laboratories, operated for the United States Department of Energy by Sandia Corporation.

Available to DOE and DOE contractors from
U.S. Department of Energy
Office of Scientific and Technical Information
P.O. Box 62
Oak Ridge, TN 37831

Telephone: (865) 576-8401
Facsimile: (865) 576-5728
E-Mail: reports@adonis.osti.gov
Online ordering: http://www.osti.gov/bridge

Available to the public from
U.S. Department of Commerce
National Technical Information Service
5285 Port Royal Rd.
Springfield, VA 22161

Telephone: (800) 553-6847
Facsimile: (703) 605-6900
E-Mail: orders@ntis.fedworld.gov
Online order: http://www.ntis.gov/help/ordermethods.asp?loc=7-4-0#online

SAND2006-6577
Unlimited Release
Printed October 2006

# A Tunable Electrochromic Fabry-Perot Filter for Adaptive Optics Applications

Daniel R. Kammler
Neutron Generator Design Science and Engineering Department

William G. Yelton, Jason C. Verley,
Photonic Microsystems Technology Department

William C. Sweatt
Applied Photonic Microsystems Department

Edwin J. Heller, Jonathan D. Blaich
MicroDevice Technologies Department

Andrea Ambrosini
Chemical and Biological Systems Department

Sandia National Laboratories
P.O. Box 5800
Albuquerque, NM 87185

*Abstract:*

*The potential for electrochromic (EC) materials to be incorporated into a Fabry-Perot (FP) filter to allow modest amounts of tuning was evaluated by both experimental methods and modeling. A combination of chemical vapor deposition (CVD), physical vapor deposition (PVD), and electrochemical methods was used to produce an EC-FP film stack consisting of an EC* $WO_3/Ta_2O_5/NiO_xH_y$ *film stack (with indium-tin-oxide electrodes) sandwiched between two* $Si_3N_4/SiO_2$ *dielectric reflector stacks. A process to produce a* $NiO_xH_y$ *charge storage layer that freed the EC stack from dependence on atmospheric humidity and allowed construction of this complex EC-FP stack was developed. The refractive index (n) and extinction coefficient (k) for each layer in the EC-FP film stack was measured between 300 and 1700 nm. A prototype EC-FP filter was produced that had a transmission at 500 nm of 36%, and a FWHM of 10 nm. A general modeling approach that takes into account the desired pass band location, pass band width, required transmission and EC optical constants in order to estimate the maximum tuning from an EC-FP filter was developed. Modeling shows that minor thickness changes in the prototype stack developed in this project should yield a filter with a transmission at 600 nm of 33% and a FWHM of 9.6*

*nm, which could be tuned to 598 nm with a FWHM of 12.1 nm and a transmission of 16%. Additional modeling shows that if the EC* $WO_3$ *absorption centers were optimized, then a shift from 600 nm to 598 nm could be made with a FWHM of 11.3 nm and a transmission of 20%. If (at 600 nm) the FWHM is decreased to 1 nm and transmission maintained at a reasonable level (e.g. 30%), only fractions of a nm of tuning would be possible with the film stack considered in this study. These tradeoffs may improve at other wavelengths or with EC materials different than those considered here. Finally, based on our limited investigation and material set, the severe absorption associated with the refractive index change suggests that incorporating EC materials into phase correcting spatial light modulators (SLMS) would allow for only negligible phase correction before transmission losses became too severe. However, we would like to emphasize that other EC materials may allow sufficient phase correction with limited absorption, which could make this approach attractive.*

# Acknowledgments

Special thanks go to Brian Brock (5731) for his support of the project and guidance in helping to define the bounds of this research. Thanks go to Michael Busse (1746) and Robert Grubbs (2452) for coordinating use of their spectroscopic ellipsometers. Thanks also to Sam Griego (24312) and Thomas Hamilton (1725) for machining shadow masks. Finally, thanks go to Gina Simpson (1822) for last minute spectroscopy measurements.

# Table of Contents

# List of Figures

Page Number

# Introduction

## Problems with narrow-band FP filters

A simple FP filter consists of a dielectric spacer material sandwiched between two reflectors. If absorption in the reflectors and dielectric spacer is ignored, then the spacing between and intensity of the transmission peaks from this optical cavity are determined by the spacing between the reflectors, the angle of incidence, and the refractive index of the spacer material, as shown in equations 1 and 2 after Yariv[1] (the impact of absorption in the reflector and dielectric spacer materials will be considered later).

$$\frac{I_t}{I_i} = \frac{(1-R)^2}{(1-R)^2 + 4R\sin^2(\delta/2)} \qquad \delta = \frac{4\pi n l \cos\theta}{\lambda} = 2m\pi \qquad \textbf{(1,2)}$$

Here $I_t$ and $I_i$ are the transmitted and incident intensities respectively. R is the reflectance of the dielectric/reflector interface, n is the refractive index of the spacer material, $\theta$ is the angle of incidence, $\lambda$ is the wavelength, l is the thickness of the spacer material, and m is an integer. A simple FP filter consisting of a dielectric 0.62 µm thick with a refractive index of 1.95 sandwiched between two reflectors (reflectance = 98%) and the corresponding transmission output is illustrated in Figs. 1 and 2 below.

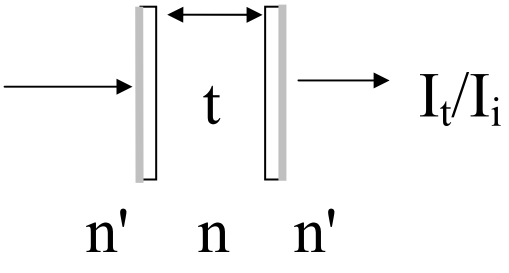

**Fig. 1 A simple Fabry-Perot Filter**

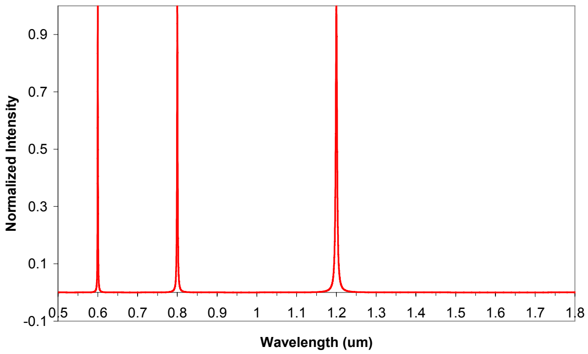

**Fig. 2 Output of a simple FP filter ($\theta_{incidence}$ =0°, t = 0.62µm, n = 1.95, r=0.98)**

Since thin film deposition techniques (CVD, PVD, etc.) used to deposit the layers in the FP filter have some inherent uniformity variation (perhaps 1-3 % across a diameter of 100 mm), the transmission peak location will also vary across the filter. Thus the larger the filter, the wider the transmission peak for a given level of nonuniformity in the deposition process. An additional problem that leads to broadening of the FP filter is temperature drift. Both thickness and refractive index will change with temperature in the dielectric material and often the two effects combine to make a larger net shift than either one alone. For example, fused silica ($SiO_2$) has a thermal expansion coefficient (CTE) of 0.5 x $10^{-6}$ 1/°C.[2] A change in temperature between 2.5 °C and 83.3 °C has been reported to yield a change in refractive index from 1.4603 to 1.4611.[3] For a 100 °C temperature swing these effects appear to be ~ 10-100 times smaller than what one would expect from uniformity variation.

# Methods of Tuning

Various methods can be used to null out the variations in optical thickness described above. Equations 1 and 2 indicate that the angle between the incident beam and the FP filter can be varied to alter the path length and shift the location of the transmission peaks. Unfortunately, this strategy works well only for a point object because any field of view will require $\theta$ in Eq. 2 to vary. This will change the transmission at the desired wavelength and the peak transmission will occur at a different wavelength for different parts of the object. Furthermore, this will not correct for variation in the thickness of the dielectric cavity over a large area due to processing non-uniformities. Changing temperature will alter the optical thickness of the dielectric because of thermal expansion, and the temperature dependence of the index of refraction. Specialized and bulky temperature control equipment must be present to use (and in some cases correct) for these effects. Again this strategy will not correct for thickness variation in the dielectric cavity across a large area. Liquid crystal (LC) materials also have refractive indices that can be varied in the presence of an electric field. Unlike EC materials, LC materials will impact the polarization state of the incident beam, and depending on the application, critical information may be lost. The materials used in an FP filter can be processed in such a way to ensure that they are all amorphous, cubic, or polycrystalline with a random in-plane texture. Consequently, there will be no in-plane (lateral dimensions of the filter) variation in refractive index and therefore, no polarization-dependent effects are introduced. Thus any polarization-based information in the signal beam will not be lost.

# EC Film stack operation and simple EC-FP filters

Since Deb[4] began investigating the solid-state color change ability of electrochromic (EC) tungsten oxide ($WO_3$) , EC materials have been incorporated into numerous devices such as "smart" windows, mirrors, and other devices that utilize its tunable absorption.[5] An electrochromic (EC) film stack consists of a set of different materials that work in concert to change color when a bias is applied across the stack. The bias drives electrochemical redox reactions that give rise to the color changes.

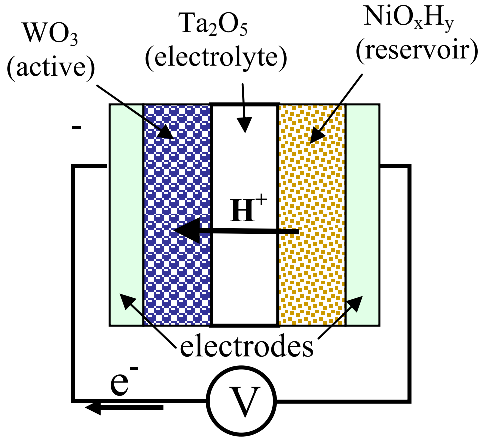

**Fig. 3 An example of an EC film stack in operation.**

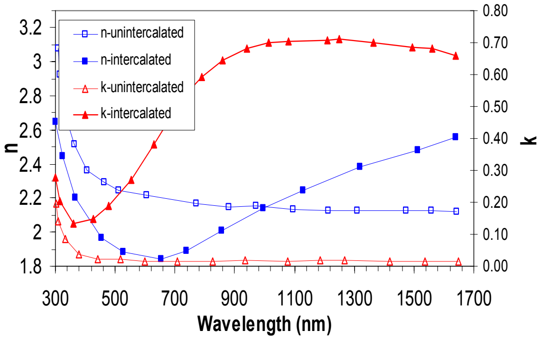

**Fig. 4 Refractive index (n) and extinction coefficient (k) of $WO_3$ before and after intercalation after Hale et al.[6]**

Fig. 3 shows a typical EC film stack that consists of a pair of transparent electrodes, an active EC material like $WO_3$ where color changes occur, a proton conducting (and electron insulating) electrolyte like $Ta_2O_5$, and a charge storage reservoir like $NiO_xH_y$ (color changes in the $NiO_xH_y$ as well).

When a potential is applied between the electrodes sandwiching the film stack as shown in Fig. 3, the $Ni^{+2}$ is oxidized to $Ni^{+3}$ and the $W^{+6}$ is reduced to $W^{+5}$ as outlined in equations 3 and 4 after Baucke.[5] While, these reversible processes give rise to changes in refractive index and absorption in both $WO_3$ and $NiO_xH_y$ films[*] (throughout the visible and infrared portions of the spectrum), the changes in the $WO_3$ film are significantly greater.[6] While traditional applications of EC materials make use of this tunable absorption, one must remember that the refractive index and extinction coefficient are coupled as described by the Kramers-Krönig relations shown in equations 5 and 6.[7] Here $\varepsilon_1$ and $\varepsilon_2$ are the real and imaginary parts of the permittivity, $\varepsilon_\infty$ is the high-frequency dielectric constant, and P denotes the Cauchy Principle Value Integral. Equations 7 and 8 relate the real and imaginary permittivity to the refractive index (n) and extinction coefficient (k). Fig. 4 shows changes in refractive index (n) and extinction coefficient (k) as a function of wavelength for $WO_3$ in both its absorbing (intercalated) and transparent (unintercalated) states.[6] While most EC applications leverage the tunable absorption to make “smart” windows, mirrors, etc., we believe the simultaneous changes in refractive index may allow creation of adaptive optics devices like large-area Fabry-Perot (FP) filters that can correct for nonuniformities introduced during processing, and the thermal drift that is a problem during operation.

$$Ni^{+2}(OH)_2^{-1} = Ni_{1-x}^{+2}\, Ni_x^{+3}\, (OH)_{2-x}^{-1}\, O_x^{-2} + xH^+ + x\, e^- \qquad \textbf{(3)}$$

$$x\, H^+ + x\, e^- + W^{+6}O_3^{-2} = H_x^+W_x^{+5} + W_{1-x}^{+6}O_3^{-2} \qquad \textbf{(4)}$$

$$\varepsilon_1(\omega) - \varepsilon_\infty = \frac{2}{\pi} \mathrm{P}\int_0^\infty \frac{\varpi'\varepsilon_2(\omega')}{\omega'^2 - \omega^2} d\omega' \qquad \varepsilon_2(\omega) = \frac{2\omega}{\pi} \mathrm{P}\int_0^\infty \frac{\varepsilon_1(\omega')}{\omega^2 - \omega'^2} d\omega' \qquad \textbf{(5,6)}$$

$$\varepsilon_1\,(\omega) = n^2 - k^2 \qquad \varepsilon_2\,(\omega) = 2nk \qquad \textbf{(7,8)}$$

We previously constructed a working tunable EC FP filter film stack similar to that shown in Fig. 3.[8] The film stack consisted of a Ti(~60Å)/Au (150 Å) back electrode, on top of which was deposited ~4000 Å of $WO_3$, ~ 3000 Å of $Ta_2O_5$, and ~ 110 Å of Au. The substrate was Pyrex. Redox chemistry involving ambient humidity that takes place at the Au/$Ta_2O_5$ interface is believed to supply the protons in this simplified EC cell.[9] The Au reflectors sandwich the simple EC cell and make a crude FP filter. Fig. 5 shows a cartoon illustrating this simple EC-PF filter and Fig. 6 shows the transmission spectra from this

---

[*] Throughout this document $NiO_xH_y$ is used to describe the continuum between NiOOH and $Ni(OH)_2$ described in Eq. 3.

device as it is cycled.  It's clear from Fig. 6 that while tuning is possible, the transmission peaks are quite broad (FWHM is ~50 nm for the peak centered at 670 nm) and the absorption associated with the tuning is severe.

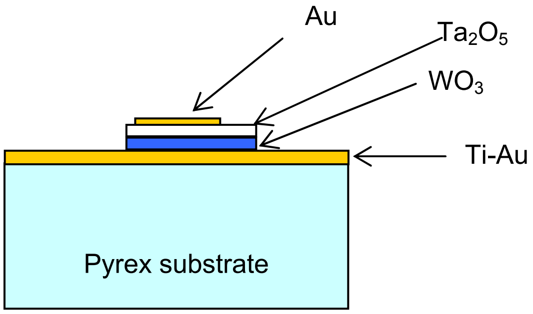

**Fig. 5 illustration of simple EC-FP filter.**

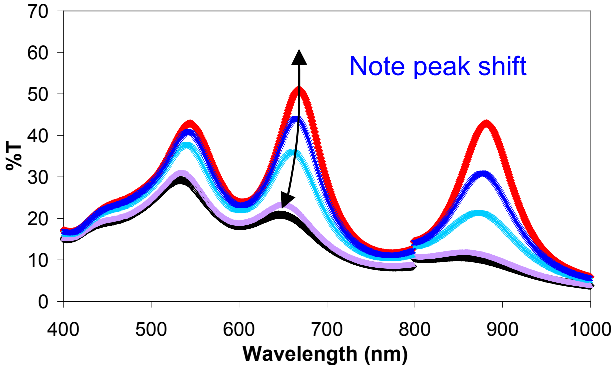

**Fig. 6 Transmission spectra from simple EC-FP filter.**

# Project Goals:

Ultimately, an FP filter with a transmission peak centered at 600 nm with a FWHM of 1 nm, a transmission of at least 30% at 600 nm and a diameter of 4 inches is desired.  Our goals are to dramatically improve on the crude EC FP filter illustrated in Figs. 5 and 6 above, provide a path to scale this technology for making large area FP filters, and evaluate whether EC materials might be incorporated into other adaptive optic devices. Specifically we wish to:

1.) Eliminate the need for ambient water (of the simple EC-FP filter shown in Fig. 5) in the atmosphere by developing a process for a $NiO_xH_y$ charge storage layer that supplies the protons needed by the $WO_3$ (as shown in Eq. 4).

2.) Dramatically reduce the FWHM and increase the intensity of the peaks in the etalon output spectrum by developing dielectric reflector stacks with high reflectance and low absorption to replace the metallic reflectors.

3.) Evaluate the extent to which it is possible to tune an EC FP filter operating at 600 nm. Can thermal drift and process uniformity be corrected using this approach?

4.) Evaluate the potential of incorporating EC materials into other devices such as phase correcting spatial light modulators (SLMS).

# EXPERIMENTAL PROCEDURE

## Process flow to produce new EC-FP film stack

Fig. 7 shows a flow chart illustrating the sequences of processes to produce the 2nd generation EC-FP filter in this project. Steps 2-6 are required to make an EC film stack and test the viability of the $NiO_xH_y$ charge storage layer and/or characterize the change in optical constants within the active layers in the cell. Skipping the additional steps (1, 7-8) which are required to make an EC-FP filter allows a quicker turn-around time to make test EC cells necessary for troubleshooting integration problems, characterizing optical constants, determining safe operating voltages, etc.

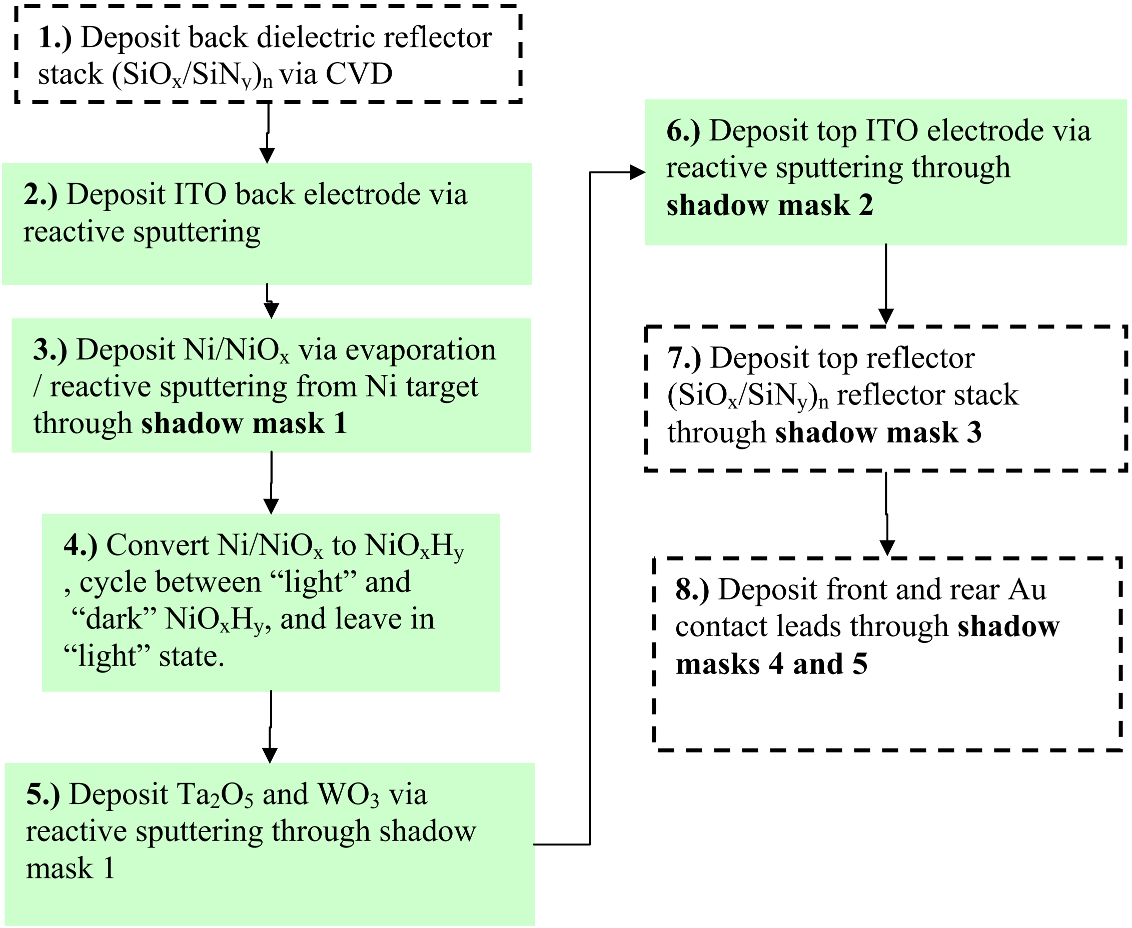

**Fig. 7 Flow chart illustrating processing sequence used to make an EC-FP filter.** All steps must be followed to make and EC-FP filter. Only steps 2-6 need be completed to make an EC test cell in order to characterize cell operation and/or troubleshoot problems.

Figs. 8a-8e show the shadow masks made from stainless steel (cleaned for vacuum service) used to pattern the different layers in the device and keep front and back contacts from shorting together. A cartoon illustrating the completed EC-FP filter device is shown in Fig. 9.

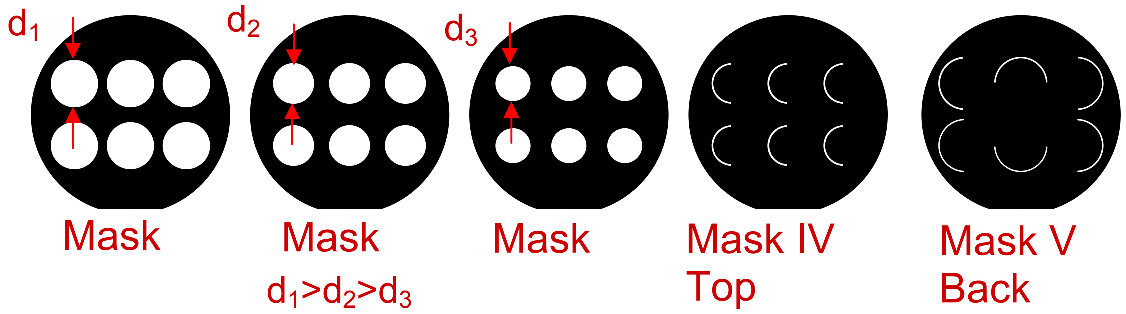

**Figs. 8a-8e. Shadow mask levels I-V used to create the EC-FP filter device in this project**

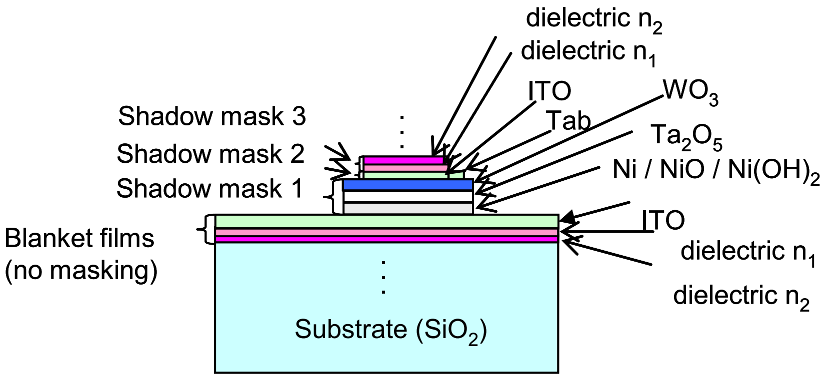

**Fig. 9 Illustration of EC-FP filter film stack.** Both top and bottom dielectric stacks could be repeated to boost reflectance.

The sizes of $d_1$, $d_2$, and $d_3$ were 1.00, 0.87, and 0.75 inches respectively.

# Thin Film Deposition Methods

## Substrate

The substrates are 3" O.D. x 0.5 mm thick Pyrex wafers ordered from Bullen Ultrasonics (Eaton, OH). 4" substrates for fabricating larger cells were also used. The wafers are used directly without further preparation.

## Plasma Enhanced Chemical Vapor Deposition (PECVD)

PECVD was used to deposit the $Si_3N_4$ and $SiO_2$ dielectric reflector layers. Three $Si_3N_4/SiO_2$ layers were deposited for each reflector (i.e. single reflector stack consisted of $Si_3N_4/SiO_2/$ $Si_3N_4/SiO_2/Si_3N_4/SiO_2$). The PECVD system is a PlasmaTherm 790. All films are deposited at 250 °C. When depositing the 3-layer pair reflector stack, vacuum is broken after the first $SiO_2$ layer and the first $Si_3N_4$ layer to measure the deposition thickness, and the final two layer pairs are deposited without opening the chamber. The deposition rates, pressures, and process chemistry for each layer are as follows:

For $SiO_2$
Rate: 160 Å/min
Pressure: 400 mTorr
Chemistry: 5%$SiH_4$ in He (60 sccm):$N_20$ (30 sccm): He (480 sccm)

For $Si_3N_4$
Rate: 90 Å/min
Pressure: 906 mTorr
Chemistry: 5% $SiH_4$ in He (120 sccm):$NH_3$ (4 sccm): $N_2$ (160 sccm): He (490 sccm)

## Sputtering of ITO, $WO_3$, $Ta_2O_5$, and $NiO_x$

DC-magnetron sputtering was used to reactively deposit indium-tin-oxide (ITO), $WO_3$, $Ta_2O_5$, and $NiO_x$. The vacuum system components were from Cooke Vacuum Products. The remainder of the components are from a variety of manufacturers (including a turbomolecular pump, a deposition rate monitor, magnetron sources, etc). Vacuum must be broken between each deposition because the sources must be covered to prevent contamination.

There are no shutters on the sources. All depositions are done with the substrate at room temperature and no DC-bias is applied. The substrate is held at system ground by the metal vacuum chamber. Background vacuum is $1 \times 10^{-7}$ Torr. All targets are 2" diameter. Target materials, deposition rates, deposition pressures, flow rates of sputter gases, and sputter deposition powers are shown for each material below:

$WO_3$: W metal target in $O_2$
Rate: 77 Å/min
Pressure: 8 mTorr
Process flows: 5 sccm Ar-20 sccm $O_2$
Sputter deposition power: 200 Watts

$Ta_2O_5$: Ta metal target in $O_2$
Rate: 250 Å/min
Pressure 4 mTorr
Process flows: 8 sccm Ar-4 sccm $O_2$
Sputter deposition power: 150 Watts

$NiO_x$: Ni metal target in $O_2$
Rate: 110 Å/min
Pressure: 6 mTorr
Process: 5 sccm Ar-20 sccm $O_2$
Sputter deposition power: 200 Watts

ITO: ITO alloy target (90 wt% $In_2O_3$-10 wt% $SnO_2$)
Rate: 535 Å/min
Pressure: 2 mTorr
Process: 8 sccm Ar
Sputter deposition power: 200 Watts
Film is annealed in air for 1 hr at 200 °C following deposition to activate the dopant

## Evaporation of Ni

The evaporator used for the Ni is a cryo-pumped bell jar system that was extensively modified. The e-beam hearth is a Temescal 10KW e-beam system. The Ni charge is made from 99.99% Ni metal. Background pressure prior to deposition was 2 x $10^{-7}$ Torr. Deposition rate is 3-5 A/sec. The substrate is held nominally at room temperature during deposition.

# Electrochemical Process to produce $NiO_xH_y$

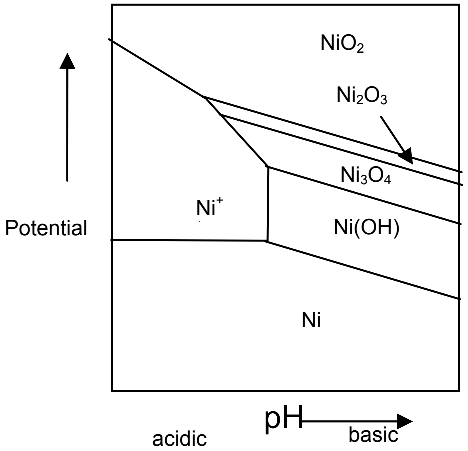

**Fig. 10 Sketch of the Pourbaix diagram for Ni in water.**

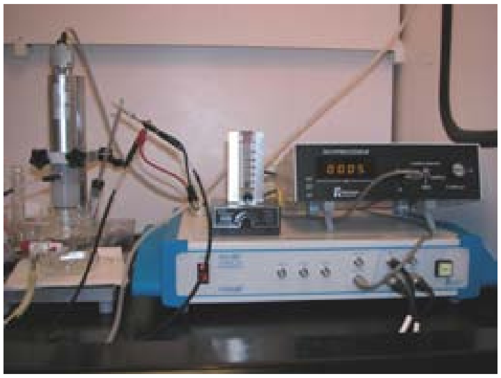

**Fig. 11 Picture of setup used to convert Ni or $NiO_x$ into the appropriate $NiO_xH_y$ state.**

As illustrated in Fig. 7, after the Ni or $NiO_x$ film is deposited via evaporation or reactive sputtering the film must be converted into the oxide/hydroxide $NiO_xH_y$ prior to completing the film stack. Both Ni and $NiO_x$ are converted to $NiO_xH_y$ electrochemically. Fig. 10 shows a sketch of the Ni Pourbaix diagram after Pourbaix[10].

Ni or $NiO_x$ films are converted to Nickel hydroxide in a solution of 0.3-0.5 M Potassium Chloride, KCl (Fisher Chemicals) with pH adjusted to >10.2 using Potassium

Hydroxide (Fisher Chemicals). All conversions to Nickel hydroxide are performed at room temperature. The KCl solution was saturated with oxygen by continuously bubbling filter air to provide higher than normal levels of oxygen. This is necessary to maintain high concentrations of oxygen at the interphase, the zone where electrochemical conversion reaction takes place between the metal/oxide interface and the solution. To drive the conversion, a VoltaLab PGZ 402 potentiostat (Radiometer Analytical) provides a constant step potential under Chrono amperometry mode, recording the current while the work potential is maintained at a preset value verse the reference potential. The potentiostat was controlled externally using VoltaMaster 4 (Radiometer Analytical, Version 4) software. For each conversion process, it was necessary to control the working potential dynamically using a three electrode cell where the solution container (304 stainless steel) served as a counter electrode, and a Saturated Calomel Electrode (SCE) provide the feedback reference. Contact to the Ni or $NiO_x$ is made through the ITO blanket back electrode (deposited just prior to the Ni or $NiO_x$ in step 2 of Fig. 7).

# EC Cell characterization and operation

Simple tests to determine whether an EC cell was functional were performed using a digital multimeter, a DC current supply, and a simple 2 point probe station to make contact with the front and back (common) electrodes. The multimeter was connected in series with the power supply and EC stack to measure current flowing in the stack as the DC voltage was stepped up. Forward or coloring mode has the negative electrode touching the top ITO electrode in Fig. 9 and the positive electrode touching the back (bottom or common) ITO electrode in Fig. 9. In bleaching mode the negative electrode is touching the back (bottom or common) ITO electrode in Fig. 9 and the positive electrode is touching the top ITO electrode in Fig. 9. Typical voltages ranged between 0 to 5 V in both coloring and bleaching modes.

# Additional Characterization techniques

## X-Ray Diffraction

The structure of the thin film was characterized by powder x-ray diffraction (PXRD) on a Siemens D500 diffractometer (Cu Kα radiation, Bragg-Brentano geometry, 5-50 deg 2-theta/5 s/ 0.05 step width) and pattern-matched using the Jade 6.5+[11] diffraction software.

## Spectroscopic Ellipsometry

The optical constants of the films used in this study were measured using spectroscopic ellipsometry. Two commercial ellipsometers were used, both made by the Woollam company. One was a VASE model, with a spectral range of ~300-1700 nm, and the other was an M-2000, with a spectral range of ~370-1675 nm. The VASE model is a rotating analyzer ellipsometer, while the M-2000 utilizes a rotating compensator. Spectroscopic ellipsometry data were collected for all the films at three angles of incidence:

either 65°, 70° and 75°, or 60°, 65° and 70°. The set of angles were selected to yield values of $\Delta$ near 90°, which gives optimal signal/noise ratio for rotating analyzer ellipsometers.

# Ellipsometry Modeling

Analysis of the spectroscopic ellipsometry data was performed with Film Wizard, a commercial optical modeling program from Scientific Computing International (SCI). The $SiO_2$ and $Si_3N_4$ film data were fitted using a Cauchy model for the real part of the index of refraction; a Cauchy model with an exponential absorption was used for the unintercalated $WO_3$; the remaining films were modeled using Lorentz Oscillators. All the samples were assumed to be homogeneous thin films on the substrate, with the exception of the ITO, which required an index gradient from the top to the bottom of the film. Figure 12 shows a fit of Psi for three angles of incidence. The lines are the best model fit to the data.

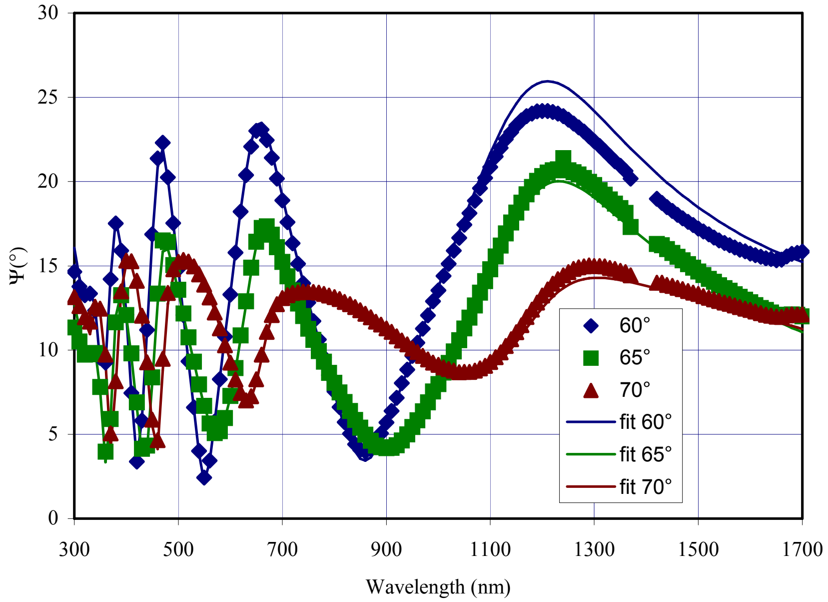

**Fig. 12 Example of Ellipsometric data best fit for ITO.** The fit is for a plot of Psi vs. wavelength.

# RESULTS AND DISCUSSION

## Characterization of the component films

### Dielectric Film Reflector Stack

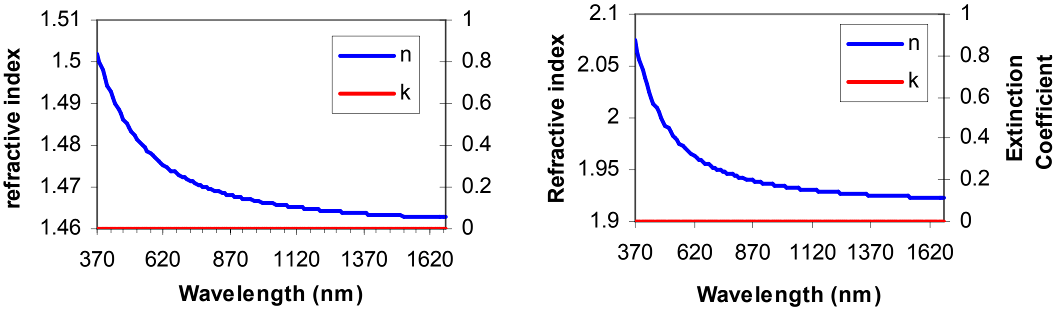

**Figs. 13a and 13b Optical constants for $SiO_2$ (13a) and $Si_3N_4$ (13b).**

Figs. 13 a and 13 b show the optical constants for the silicon oxide and silicon nitride, respectively, which make up the dielectric reflector stack. Both films have no measurable absorption (i.e. k=0) over all the wavelengths investigated. At 600 nm the silicon oxide film has a refractive index of 1.476 and the silicon nitride has a refractive index of 1.967.

### ITO

As noted in the experimental section, the ITO films were annealed as part of the processing. This anneal decreased the sheet resistance in a 3000 Å film from 1000 to 150 Ω/square. This is probably a result of an increased carrier concentration after the anneal that is a consequence of reducing some defect complexes present in the ITO.[12,13] Fig. 14 shows the spectroscopic ellipsometry data collected from a 3000 Å ITO film following the standard 200 °C 1 hr. vacuum anneal. Modeling the optical constants in ITO can be challenging since refractive index and extinction coefficients are known to vary throughout the film depth.[14,15] The two extremes along the gradient present in our films are shown.

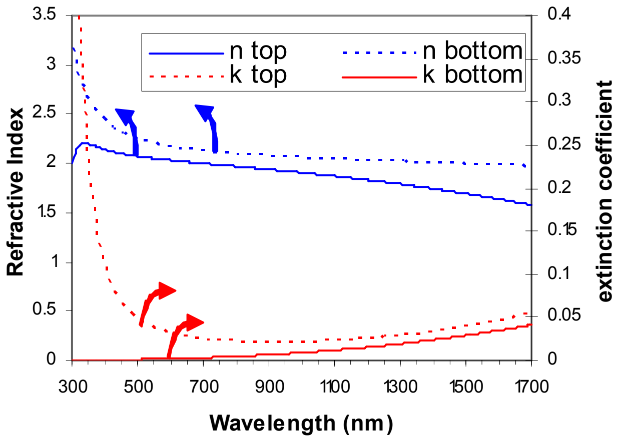

**Fig. 14 Measured optical constants for ITO films used in this study**

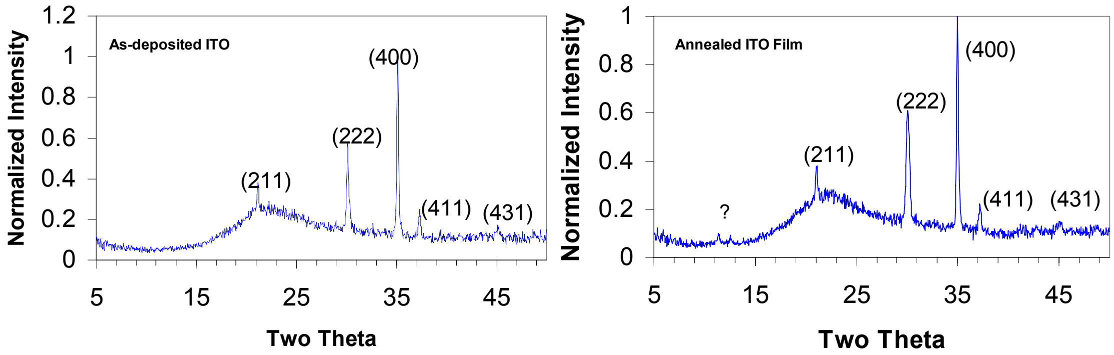

**Figs. 15a and 15 b. XRD pattern of ITO films on Pyrex before and after a 1 hr. anneal at 200 °C in vacuum.**

Both n and k change rapidly at short wavelengths near the optical band gap for ITO. Figs. 15a and 15b show XRD data before and after the 200 °C 1 hour anneal. All the major peaks in the both the as-deposited and annealed samples belong to the cubic bixbyite phase of indium oxide.[16] A couple of smaller peaks at low angle in the annealed specimen could be from a small quantity of impurity phase or perhaps some instrumental artifact (e.g. sample holder is being caught in the beam).

## $WO_3$

Figs. 16 and 17 show spectroscopic ellipsometry and XRD data for the $WO_3$ films produced via the reactive sputtering process described in the experimental section.

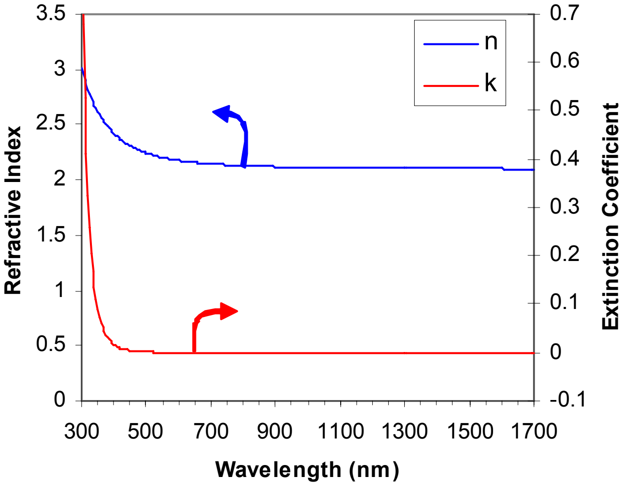

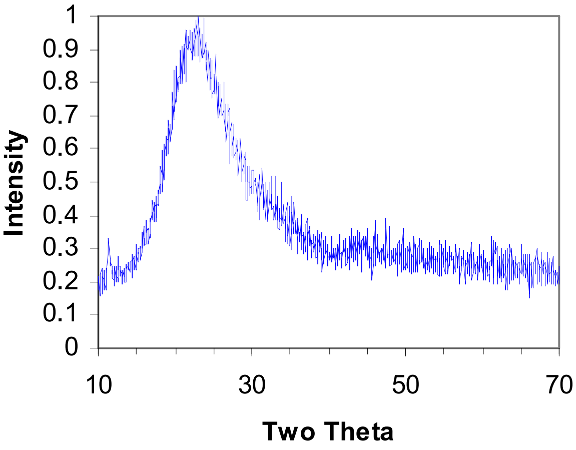

**Fig. 16 Optical constants for as-deposited $WO_3$.**

**Fig. 17 XRD pattern of as-deposited $WO_3$ (1400 Å) film on Pyrex.**

It is apparent from the low k that the as-deposited $WO_3$ is transparent with a refractive index between 2.1 and 2.2 for most of the measured wavelength range. Both change rapidly at shorter wavelengths as the indirect band gap is approached[17]. The XRD pattern shows only a broad hump centered at ~ 23° two theta which indicates the $WO_3$ film is amorphous. While heating amorphous $WO_3$ films above 385°C has been shown to begin the crystallization transformation[18], the fact that these films never exceed 250 °C (during the deposition of the $SiO_2/Si_3N_4$ top reflector stack) insures they will remain in the amorphous state. Consequently, although the refractive index may be changing significantly in this layer during operation, it cannot impact the polarization state of the incident light wave.

## $Ta_2O_5$

Figs. 18 and 19 show spectroscopic ellipsometry and XRD data for the as-deposited $Ta_2O_5$ $H^+$ electrolyte films produced in this study.

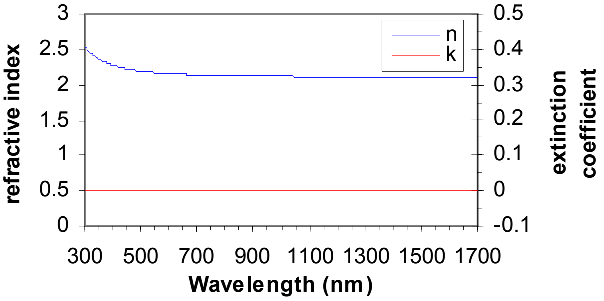

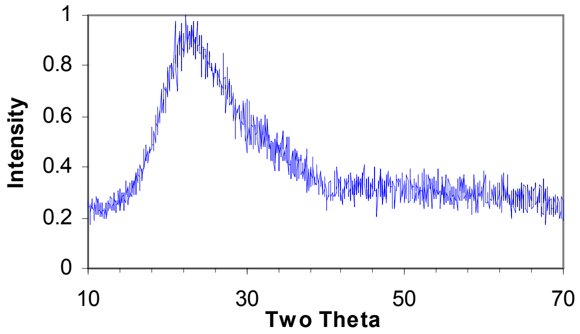

**Fig. 18 Optical constants for as-deposited $Ta_2O_5$**

**Fig. 19 XRD pattern of as-deposited $Ta_2O_5$ (3050 Å thick) film on Pyrex**

The absorption is zero throughout the measurement range and the refractive index is between 2.1 and 2.2 over the range of interest. At a wavelength of 600 nm, n = 2.157. The XRD pattern in Fig. 19 shows only a broad hump centered around ~22.5 ° two theta indicating the $Ta_2O_5$ is also amorphous.

## $NiO_x$ [*]

As noted in the experimental section nickel oxide films were reactively sputtered from a Ni target and subsequently converted into the hydroxide via electrochemical means.

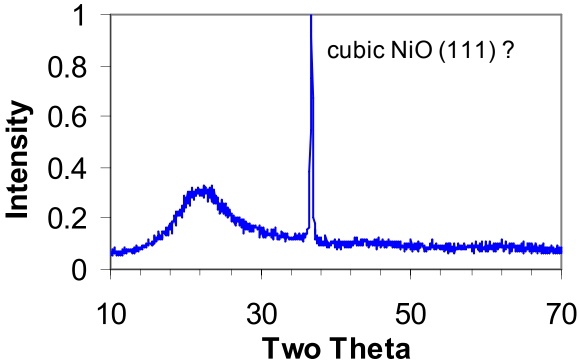

**Fig. 20 XRD pattern of as-deposited NiO (2600 Å thick) on Pyrex**

Fig. 20 shows the XRD pattern of the initial as-deposited $NiO_x$ film prior to electrochemical conversion into the hydroxide charge storage layer. There is an amorphous hump near 22 ° two theta and one very strong peak at 36.75 ° two theta that can be indexed to the (111) peak of FCC cubic NiO. If the peak belongs to cubic NiO, then the cell constant would be 4.24 Å.

# Charge Storage Layer development

As noted in Fig. 7, creation of the $NiO_xH_y$ charge storage layer is a two-part process. First the as-deposited elemental Ni (produced via evaporation) or $NiO_x$ (produced via reactive sputtering) must be converted into $NiO_xHy$. Then the film is cycled back and forth along the continuum between NiOOH and $Ni(OH)_2$ so that visible color changes are observed. The hydroxide end of the continuum is lighter in color and the oxide/hydroxide end is darker in color. The films are left in the "light" state prior to completing the rest of the layers in the film stack as shown in Fig. 7. Since there is a continuum between the oxide and hydroxide and it is difficult to say exactly where along the continuum the film is; we use the convention "light" and "dark" $NiO_xH_y$. The process details of these steps are reported below.

---

[*] No characterization of the evaporated elemental Ni films was done.

## Conversion of elemental Ni into $NiO_xH_y$

Nickel metal films are converted to nickel hydroxide in a solution of 0.5 M potassium chloride with pH adjusted to >10.2 using potassium hydroxide. To convert nickel metal to nickel hydroxide a continuous positive potential from +800 to +1500 mV vs. SCE [244 mV vs. Normal Hydrogen Electrode (NHE)] for 60 to 600 minutes was required. At a solution pH below 10, the nickel metal reaction kinetics were so sluggish that conversion was not possible within a 24 hour period. At a solution pH greater than 10 the conversion formed from the nucleating site outward. The conversion was not driven directly by current flux alone, but "grew" from various spots on the wafer until the spread of the hydroxide conversions overlapped one another. This process was slow, often taking 6 or more hours. At pH values greater than 10 but less than 12, the process was faster, often taking less than an hour. And at pH values greater than 12, the film dissolved. During conversion, if using nitrogen instead of air under normal operating pH values, the reaction was kinetically slow, often not fully converting over a 6 hour period.

Although the films produced using this process are functional, they appear grainy and reticulated to the eye, suggesting that the surface of these films may be quite rough. Fig. 21 shows a scanned image of step profilometer data from an $NiO_xH_y$ film surface that was created electrochemically using the above process. Features over 5 kÅ tall are observed. The film stack started as glass/ITO/Ni and was converted to glass/ITO/$NiO_xH_y$. Perhaps the stress of incorporating both hydrogen and oxygen into the elemental Ni film to produce the $NiO_xH_y$ charge storage layer is responsible for this problem. Conformal coating of such features with the subsequent layers in the EC stack ($Ta_2O_5$, $WO_3$, ITO) would be difficult. Since these features may lead to shorting across the stack, an alternative method of producing the charge storage $NiO_xH_y$ layer became necessary.

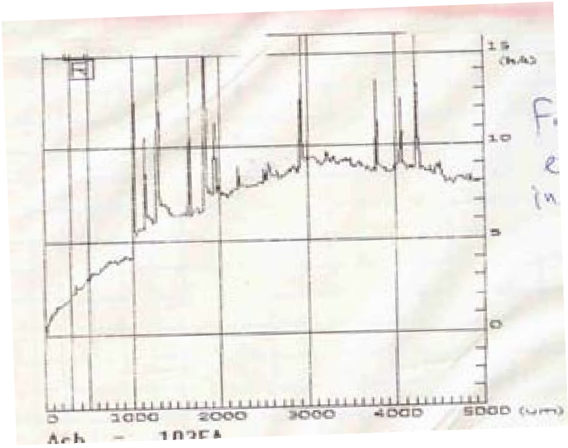

**Fig. 21 Step profilometer measurement of a glass/ITO/$NiO_xH_y$ film stack.** Units of y-axis are kÅ. Units of x-axis are µm.

## Conversion of $NiO_x$ into $NiO_xH_y$

To convert the sputtered $NiO_x$ to $NiO_xH_y$, a continuous negative potential from -400 to -1000 mV vs. SCE [244 mV vs. Normal Hydrogen Electrode (NHE)] for 20 to 60 minutes was required. At pH levels below 10, the nickel oxide reaction kinetics were too sluggish to convert the nickel oxide to hydroxide within a 5 hour period. At pH levels below 7, the nickel oxide dissolved. At a solution pH greater than 10.2, the conversion of nickel oxides to nickel hydroxides was fast, often taken place within 5 minutes under reducing potentials. After 20 minutes or more the current during the formation of the hydroxide film became steady. Often, the oxide/hydroxide conversion from the oxide required higher than normal thermodynamic potentials in order to drive the electrochemical kinetics. If the reduction potentials are too high, greater than 1.0 V DC vs. SCE for thin films( ca. 20 to 200 nm films), the film stripped and nickel metal redeposited near the solution-to-air interface of the wafer.

The $NiO_xH_y$ films produced in this way were much smoother than those produced from elemental Ni. Fig. 22 shows a step profilometer measurement of a glass/ITO/$NiO_xH_y$ film stack after the electrochemical conversion of the sputtered $NiO_x$ film. Features are 10s of angstroms tall.

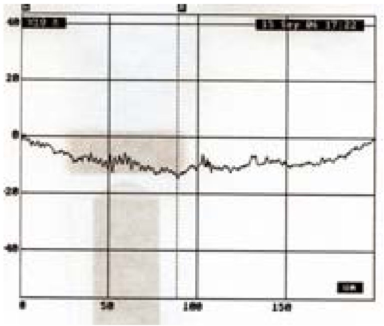

**Fig. 22 Step profilometer line scan over the top of a Glass/ITO/$NiO_xH_y$ specimen produced from sputtered $NiO_x$ .** The x-axis is in microns and the y-axis is in 10s of Å.

## Switching between light and dark $NiO_xH_y$

To demonstrate whether the Ni/$NiO_x$ conversion to $NiO_xH_y$ was successful, the cell was switched between the light and dark modes. Cells that did not switch were not used. The experimental setup for this test was similar to that used to convert Ni/$NiO_x$ to $NiO_xH_y$. Each switching test takes place in 0.3 M KCl solution at room temperature. Air agitation was used to stir the solution, but was not necessary. Mode switching was also possible in a stagnate solution. The electrochemical cell consisted of a three-electrode system, where the working electrode was the nickel film, the counter was either Pt mesh or a SS beaker, and the reference was SCE. The pH of the solution was not adjusted after KCl was added. Typical pH values for the solution was ~ 7. Under Chrono amperometry mode, the potential was switched between +1.0 V to -1.0 V for a given period of time. Figure 23 is an example of a quarter-wafer changing from light to dark as a function of potential. In the light mode, when the potential was driven cathodically, after a few seconds the wafer became nearly transparent. When the potential was switched to the anodic mode (positive current), after a few seconds the wafer darkened as seen in the example in Fig. 23. During the switching modes, the currents reach a maximum value in seconds and then decay exponentially to equilibrium levels within 10 to 30 seconds. Interestingly, the maximum anodic current (positive values) used to darken the cell was about half the maximum of the cathodic current used to lighten the cell. After the end of each cycle, the equilibrium current under the anode mode was a fraction of the equilibrium current in the cathode mode. This accounts for the higher impedance necessary to convert the cell to the dark mode, as compared to the reverse reaction in the light mode. After cycling the cell 100 times the switching currents appeared the same.

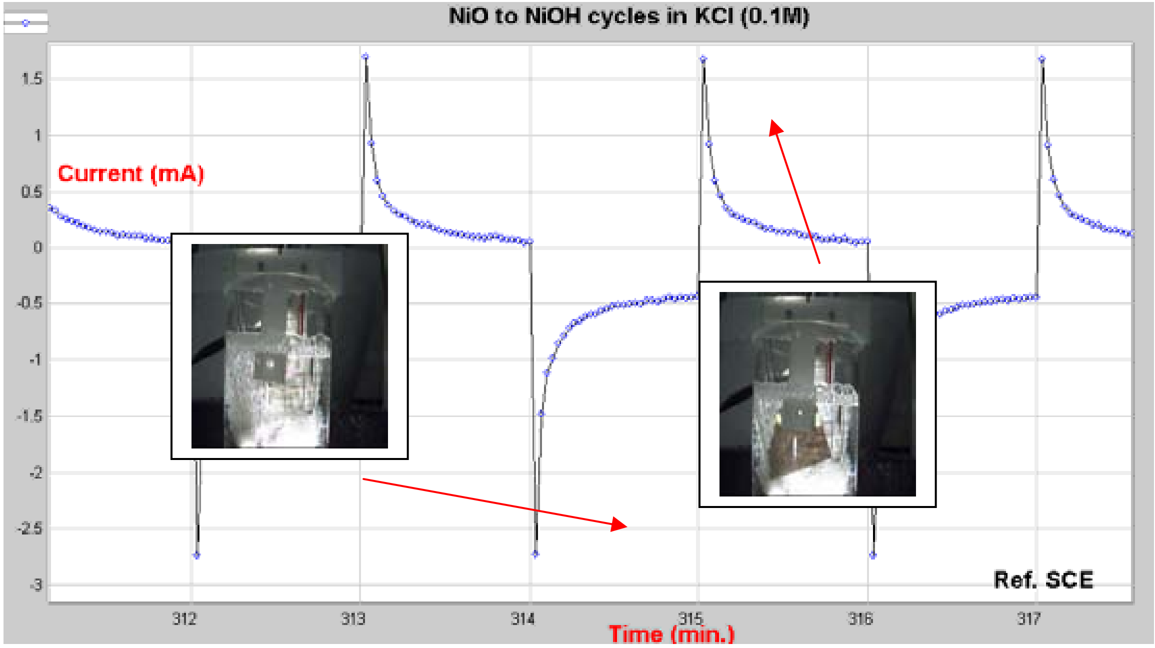

**Fig. 23 Switching between light and dark $NiO_xH_y$ in 0.3 M KCl, pH 7.** The potential (vs. SCE, sat. KCl) is switch between +1.0 V to -1.0 V for 60 seconds. Interestingly, the cathodic current flow is greater at -1.0 V as compared to the anodic current at +1.0 V to darken the wafer. The reaction to darken has a greater impedance than that to lighten.

Figs. 24 and 25 show XRD patterns of the $NiO_xH_y$ after electrochemical processing when in the light (intercalated) and dark (unintercalated) states, respectively.

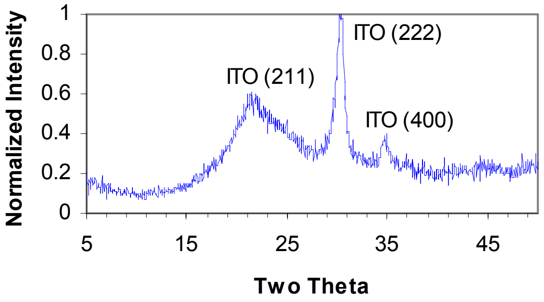

**Fig. 24 XRD pattern of the sputtered NiO film on ITO coated class after electrochemical treatment to leave the $NiO_xH_y$ film in the light state.**

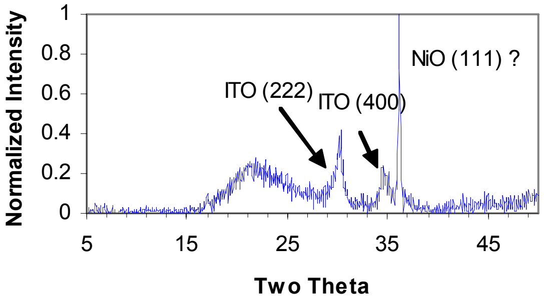

**Fig. 25 XRD pattern of the sputtered NiO film on ITO coated class after electrochemical treatment to leave the $NiO_xH_y$ film in the dark state.**

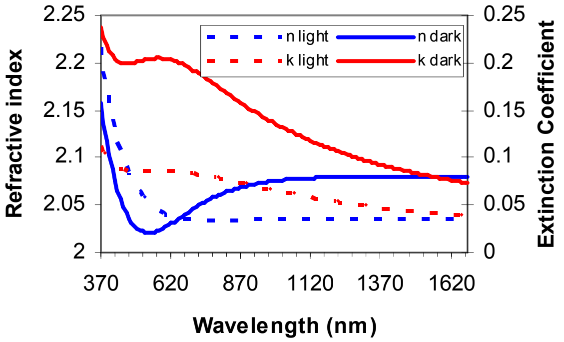

**Fig. 26 Optical Constants for "light" and "dark" $NiO_xH_y$.**
Film stack was glass/TiAu(150 Å/2 kÅ)/$NiO_xH_y$ (2 kÅ)

The $NiO_xH_y$ film in Fig. 24 appears to be amorphous. The only peaks present belong to the ITO electrode. In contrast, Fig. 25 shows one strong peak that might belong to the (111) peak of the $NiO_x$ phase in Fig. 20.[¥] Fig. 26 shows the optical constants for the $NiO_xH_y$ in both the light and dark states. Compared to the changes in $WO_3$ shown in Fig. 4, the changes in the $NiO_xH_y$ are small. However, "light" $NiO_xH_y$ has a significant level of absorption while unintercalated $WO_3$ has almost no absorption.

---

[¥] If this phase turns out NOT to be cubic, possesses an "in-plane" texture, and has grains larger than the 600 nm wavelength of interest then it's possible it may measurably alter the polarization state of the incoming beam as this phase is formed (during cell operation). In this case additional materials process optimization may be necessary to ensure at least one of these three conditions is not met in the $NiO_xH_y$ charge storage layer.

# Integration of charge storage layer into EC stack

Initial attempts to incorporate the new $NiO_xH_y$ charge storage layer (created by electrochemical conversion of elemental Ni) proved unsuccessful. Fig. 27 shows the current passing through an EC cell consisting of glass/ITO (2000 Å)/$NiO_xH_y$ (200 Å)/$Ta_2O_5$ (3000 Å)/$WO_3$ (3800 Å)/ITO (2500 Å) as the potential is ramped up to 3 V[§]. The $NiO_xH_y$ layer was created by electrochemical conversion of a 200 Å thick elemental Ni film deposited via evaporation. The I-V behavior appears to be ohmic, and suggests the presence of a short. Fig. 28 shows a step profilometer scan of the complete film stack. Large features nearly 1 μm tall are present over the top of the EC cell. This suggests the features observed in the $NiO_xH_y$ films converted from elemental Ni (see Fig. 21) were translated up through the remaining layers in the film stack and are the cause of the apparent electrical shorting.

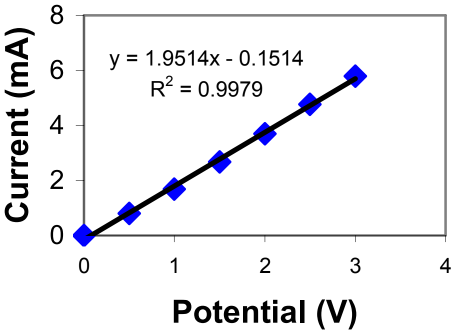

**Fig. 27 IV sweep of EC cell containing charge storage layer produced from elemental Ni.**

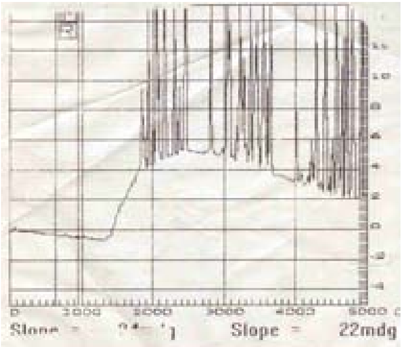

**Fig. 28 Step profilometer line scan over top of cell used to generate the data in Fig. 27.**
Units of x-axis are μm. Units of y-axis are kÅ.

Later attempts at making an EC cell incorporating the new $NiO_xH_y$ charge storage layer (created by conversion of reactively sputtered $NiO_x$) were successful. Figs. 29a-c show a cell consisting of glass/ITO(2500 Å)/$NiO_xH_y$(3200 Å)/$Ta_2O_5$ (2800 Å)/$WO_3$ (3900 Å)/ITO(2200 Å) as the cell is colored (top ITO electrode biased negative relative to the back common electrode) and bleached (top ITO electrode biased positive relative to the back common electrode). Fig. 30 shows an I-V sweep of a cell on this wafer. This time the current rises exponentially with applied potential.[§§] Fig. 31 shows a step profilometer line scan over an EC cell produced using the $NiO_xH_y$ made from sputtered $NiO_x$. The sharp features present in the EC cell with $NiO_xH_y$ made from elemental Ni (Fig. 28) are absent. This appears to have solved the shorting problem.

---

[§] This is the steady state current. No decay or change in current was observed with time.

[§§] The current actually decayed with time on this cell. The numbers shown represent the initial current observed as the potential was stepped up.

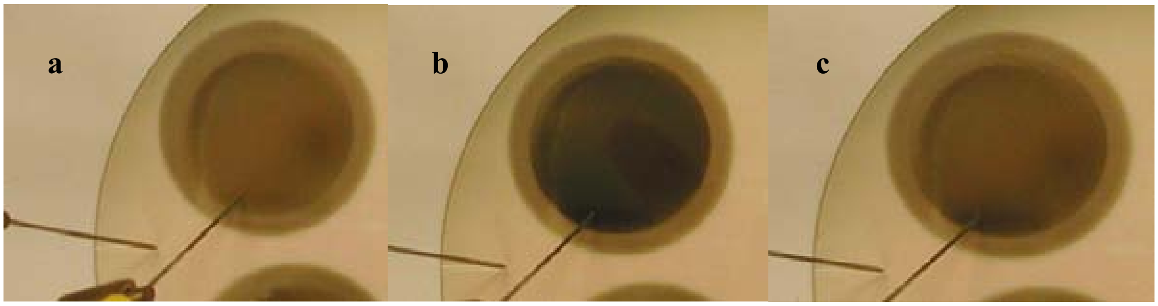

**Figs. 29a-c pictures of operational EC cell consisting of glass / ITO(2500 Å) / $NiO_xH_y$(3200 Å) / $Ta_2O_5$ (2800 Å) /$WO_3$ (3900 Å) / ITO (2200 Å) as the cell is cycled between coloring and bleaching modes.** Cell diameter is 1".

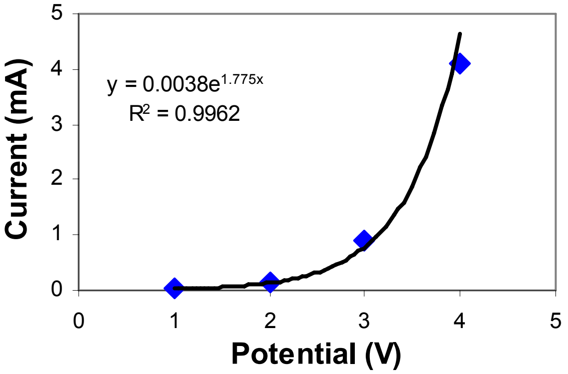

**Fig. 30 I-V sweep of EC cell containing $NiO_xH_y$ charge storage layer produced from reactively sputtered $NiO_x$.**

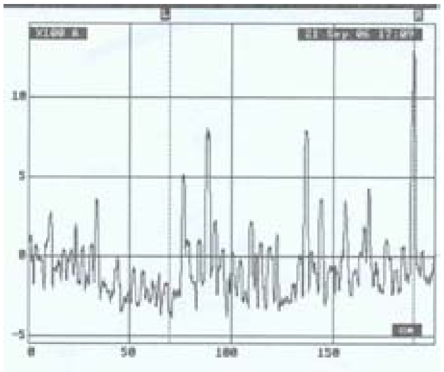

**Fig. 31 Step profilometer line scan over the top of a Glass/ITO/$NiO_xH_y$/$Ta_2O_5$/$WO_3$/ITO specimen produced using the sputtered $NiO_x$ .** The x-axis is in microns and the y-axis is in 100s of Å.

# Integration of EC stack into FP filter

Initial attempts at producing the $Si_3N_4$/$SiO_2$ dielectric reflector stack on top of ITO-coated glass lead to severe cracking in the reflector stack. Since the first process used to produce the $SiO_2$ films was a PETEOS process that took place at 375°C, thermal mismatch between the oxide, nitride, and/or ITO/substrate seemed to be a possible candidate for the cracking mechanism. Changing to a silane based PECVD chemistry allowed for the temperature to be decreased to 250 °C (the same temperature as the $Si_3N_4$ process). Following this process change the reflector stack could be produced crack free.

At this point, the entire EC-FP filter film stack illustrated in Fig. 9 could be produced. A first attempt at making the entire stack incorporated the $NiO_xH_y$ film created from elemental Ni. The EC cell inside the EC-FP stack would not function (it was probably severely cracked and delaminated like the film from Fig. 21, which lead to shorting of the front and back electrodes). Fig. 32 shows a plot of the transmission through one of theses complex EC-FP cells.

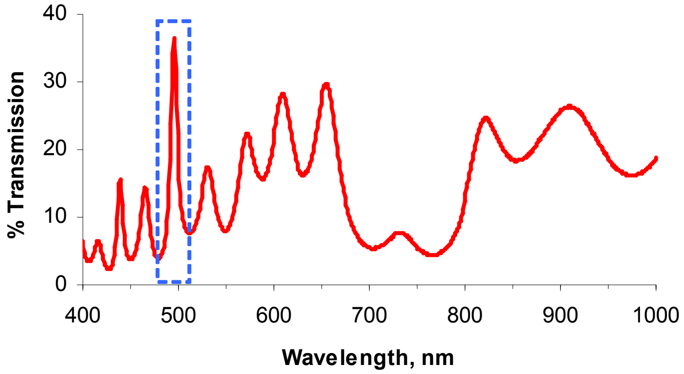

**Fig. 32 Transmission vs. wavelength for EC-FP filter incorporating charge storage layer and dielectric reflector stacks.** Film stack is: Glass/$(Si_3N_4/SiO_2)_3$/ITO/$NiO_xH_y$/$Ta_2O_5$/$WO_3$/ITO/$(Si_3N_4/SiO_2)_3$

The film stack in Fig. 32 is as follows: Glass/[$Si_3N_4$(750Å)/$SiO_2$(1000Å)]$_3$/ITO(3600 Å)/$NiO_xH_y$(200 Å)/$Ta_2O_5$(2900 Å)/$WO_3$(4700 Å)/ITO(2500 Å)/[$SiO_2$(1000 Å)/$Si_3N_4$(750Å)]$_3$. The transmission spectrum in Fig. 32 confirms the effectiveness of the dielectric reflector stack at reducing FWHM. The crude EC-FP filter in Fig. 6 had a FWHM of ~ 50 nm for the peak centered near 670 nm. The peak centered near 500 nm in Fig. 32 has a FWHM of ~ 10 nm (inside blue dashed box). Further reduction in FWHM could be achieved by increasing the number of reflector layers ($Si_3N_4$/$SiO_2$), and/or increasing the thickness of the EC material stack inside the reflectors. The tradeoffs associated with these changes are discussed in the modeling section that follows. The peak transmission in this stack may be reduced significantly by diffuse scattering off the cracked and delaminated $NiO_xH_y$ charge storage layer. If the cracking in the $NiO_xH_y$ layer inhibited the conversion process and elemental Ni is present, absorption from the Ni is probably also reducing transmission through the stack in Fig. 32.

The process changes in the $NiO_xH_y$ layer described in the "Integration of charge storage layer into EC stack" section solved the problems in the EC stack (figs. 26a-c show a working EC stack incorporating this film). As of the writing of this SAND report, time has run out to incorporate the working EC stack into the entire complex EC-FP filter.

# Modeling of EC FP Filters

## Losses due to EC materials in an Etalon Cavity

### Background and underlying assumptions

Simple FP filters were described in the Introduction. We now consider the effect of absorption in the dielectric spacer material. Inserting an electrochromic (EC) material into the etalon's cavity enables a small amount (~1 nm) of wavelength tuning to accommodate temperature changes in the etalon and small wavelength drifts in laser sources.

Nothing comes for free. If the index of refraction of the EC material is changed, there will be a change in the material's absorption. This absorption will reduce the etalon's peak transmission and increase the full-width, half-max (FWHM) of its pass band. The absorption/refractive index relationship can be quantitatively studied using the Kramers-Krönig relations (see equations 5 & 6).

Etalons can act as narrow-band filters if the two reflective surfaces each have a high reflectance—typically R > 90%. This causes the light at the resonant wavelength to bounce back and forth in the cavity many times. Each time the light bounces off the output reflector (the second one), some light (at the resonant wavelength) exits the cavity in phase with previous contributions. Many exiting beamlets from many bounces add together coherently, resulting in a high transmission at the resonant wavelength. Clearly, absorption within the cavity will diminish the amplitude of the exiting beamlets and thus the transmission of the filter.

We have tried to compute the effect of absorption by the EC material in a way that would be useful to a user of the technology. We assume that the user will know the wavelength of operation ($\lambda$) and the desired spectral width (FWHM) of the filter. Furthermore, the user will know what minimum transmission will be required at the resonant wavelength. It is assumed that the thickness of the EC material and the reflectance of the reflective surfaces are available parameters. We allow these parameters to vary, searching for a maximum absorption of the EC material that fits the peak transmission and FWHM requirements. Allowing the absorption to vary up to this maximum value enables the greatest change of refractive index in the EC material. This is equivalent to allowing the greatest change in the cavity's resonant wavelength.

The optimal cavity thickness is often several wavelengths thick, which means that there can be many resonant transmission peaks. This requires that a fairly wide band-pass filter needs to be used in conjunction with the narrow-band etalon. This wide-band filter will typically have a transmission >90% and its pass-band should be very insensitive to temperature variations. It should be slightly tilted relative to the etalon to avoid cross-talk.

Reflective coatings absorb and/or scatter a small fraction of any light incident on them. Of the possible metal coatings, silver is the best, and it will absorb a few percent. Dielectric coatings are better. The combined absorption and scatter of a dielectric coating can be a few tenths of a percent. We assumed there is no absorption in the reflector stack.

## Summary of the results

Figure 33 shows an etalon with multiple beamlets transmitting through the second reflective surface. Equations (12a)-(12d) describe the intensity of the beam transmitted through an etalon. Figures 34, 35, and 36 are plots of the absorption versus the etalon's cavity thickness for two transmissions, $T_{peak}$ = 30% and 75%, and filter widths of FWHM = 1 nm and 10 nm. Note that there are several curves on each plot that represent variations in the free spectral range (FSR). To generate these plots, we had to choose a resonant wavelength for the cavity ($\lambda$=600 nm) and an absorption (A=0) for the reflectors. From the plots the maximum allowable amount of absorption in the EC material ($\alpha$ ) increases as the reduced thickness decreases. For all of these parameters, and assuming a reasonable film thickness of >50 nm, the maximum absorption in the EC material is on the order of $\alpha \sim 10\ \mu m^{-1}$.

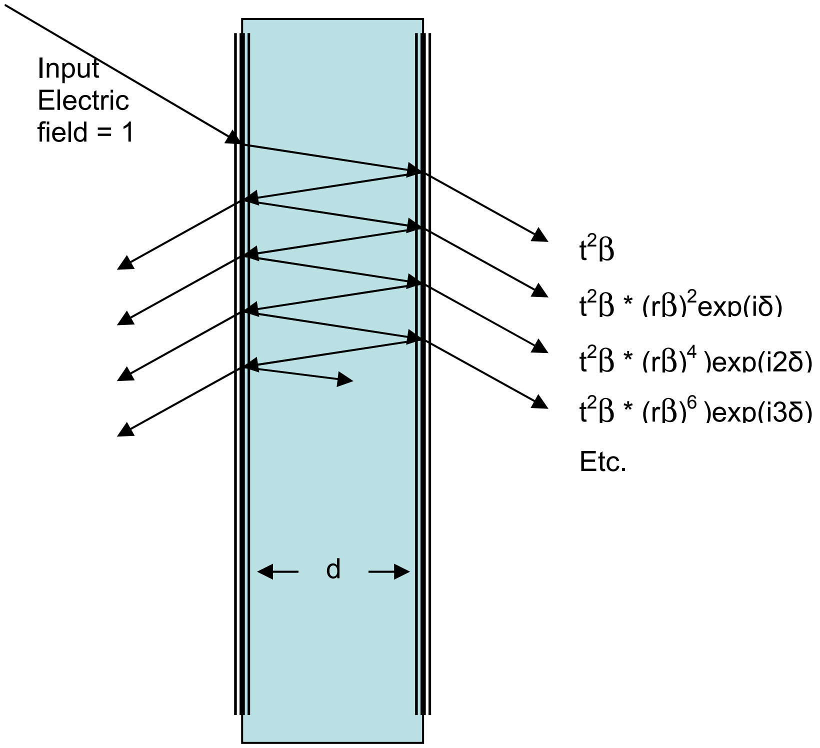

**Fig. 33: Transmitted beams through an etalon in terms of electric field.**

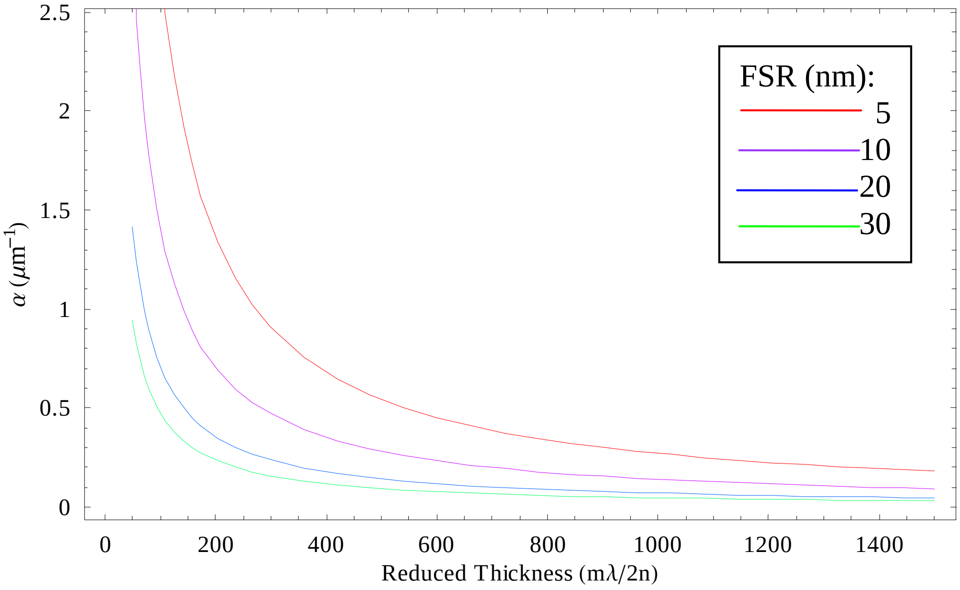

**Fig. 34: Absorption vs. reduced thickness for $T_{max}$ =30%, A=0, FWHM = 1 nm, $\lambda$ = 600 nm**
Reduced thickness has units of nm.

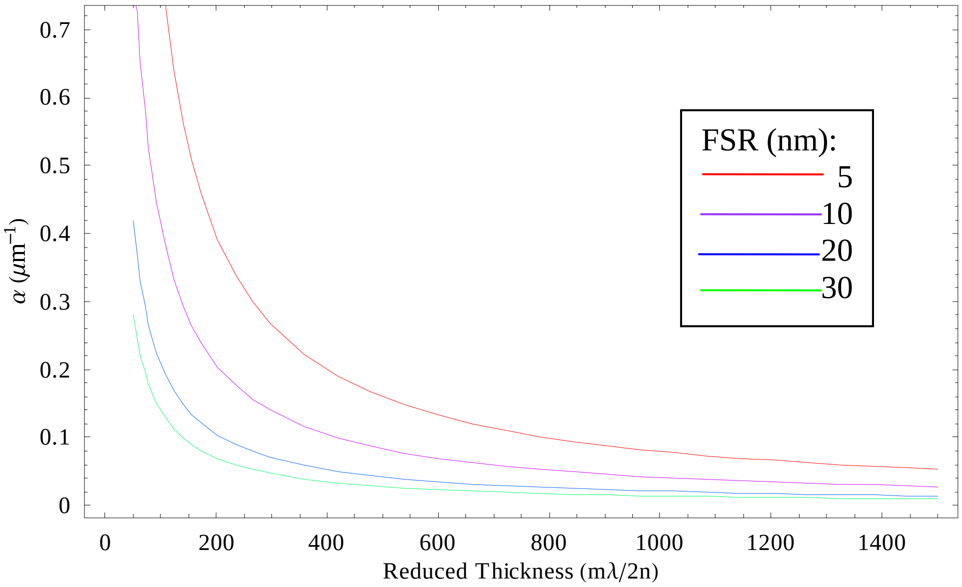

**Fig. 35: Absorption vs. reduced thickness for $T_{max}$ =75%, A=0 FWHM = 1 nm, λ = 600 nm** Reduced thickness has units of nm.

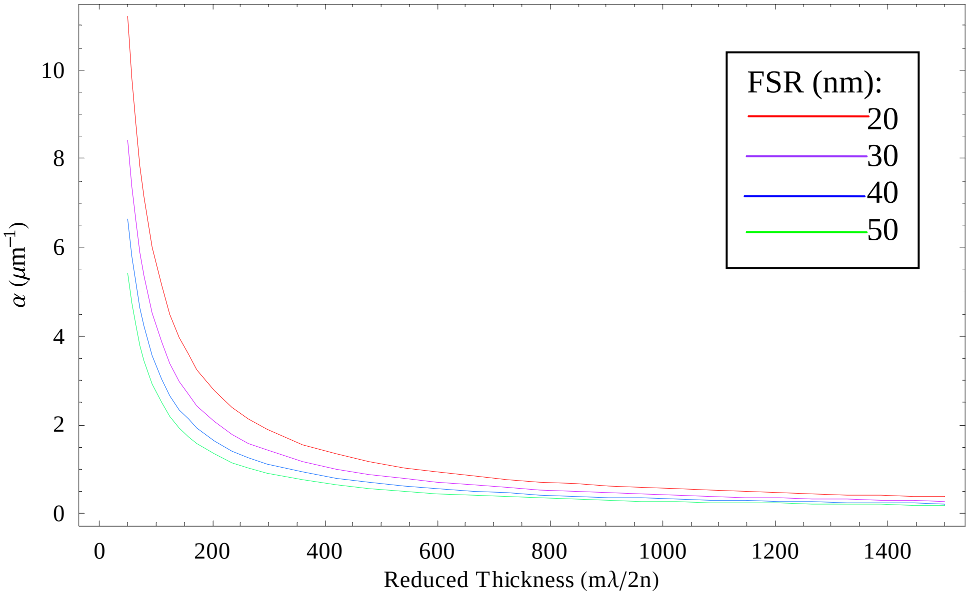

**Fig. 36: Absorption vs. reduced thickness for $T_{max}$ =30%, A=0 FWHM = 10 nm, λ = 600 nm** Reduced thickness has units of nm.

## The analysis

We will first sketch out the development of the equation for the total transmission of the etalon. Figure 33 shows the beamlets exiting the back side of the etalon. We have to do this calculation as a function of the amplitude of the electric field. Note that, for simplicity, the input is assumed to be unity. The first transmitted beamlet is reduced by $t^2 \beta$, where t is the transmission of one of the reflective coatings described in terms of amplitude, not intensity. $\beta$ (again in amplitude terms) is related to the absorption of the EC material, which is explained below. The next beamlet is further reduced by $r^2$, and its phase differs from the first beamlet by $\delta$. The rest of the beamlets follow the same pattern.

The electric field transmitted through the etalon is simply the sum of the beamlets. This sum is an infinite series, which can be converted to:

$$E = t^2\beta \,/\, \{1 + (r\beta)^2 \exp(i\delta)\} \qquad \textbf{(9)}$$

We need to convert the electric field into intensity, which is the electric field multiplied by its complex conjugate:

$$I = E \cdot E^* \qquad \textbf{(10)}$$

Also, the amplitude-based r and t must be converted into intensity-based values. From the law of conservation of energy, we know that:

$$R + T + A \equiv 1, \qquad \textbf{(11)}$$

where the capital letters relate to intensity. The absorption of the EC material is 1-B, where $B = \beta^2$. Solving equations (9)-(11) yields:

$$I = B\{(1-R-A)/(1-RB)\}^2 * \{1+ F*\sin^2(2\pi nd/\lambda)\}^{-1}, \qquad \textbf{(12a)}$$

where the “coefficient of finesse” is

$$F = 4BR \,/\, (1-BR)^2, \qquad \textbf{(12b)}$$

the phase term is

$$\delta = 2\pi nd/\lambda, \qquad \textbf{(12c)}$$

and the transmission of the EC material in the presence of absorption is:

$$B = \exp[-\alpha d\,]. \qquad \textbf{(12d)}$$

The thickness of the etalon is d, the real part of the index of refraction is n, and $\alpha$ is the absorption coefficient.

### Calculating the optimal cavity

Equation (12a) contains all the information that we need to design an optimized cavity. The full-width, half-max is determined by setting the transmission equal to half of its peak value and looking for the change required in the wavelength $\lambda$.

$$\mathrm{FWHM} = 4 / \sqrt{F} \quad [\text{radians}], \qquad \textbf{(13)}$$

thus F [Eq. (12b) ] is defined.

From (12a) the peak transmission, occurring at $\lambda_{max}$, is

$$T_{peak} = B\{(1-R-A)/(1-RB)\}^2 \qquad \textbf{(14)}$$

This occurs when $\delta = 2\pi m$, where m is an integer. Solving Eqs. (12) – (14) together, we can derive R and B (and thus $\alpha$) as a function of $T_{peak}$, A, $\lambda_{max}$, the free spectral range and the thickness of the etalon.

There are now enough relationships to numerically study the maximum allowable absorption $\alpha$ that will give the *FWHM* and $T_{peak}$ for a given coating absorption *A*; and of course, given the maximum $\alpha$, one can calculate the greatest change in refractive index for the electrochromic etalon cavity.

In Figs. 34, 35, & 36 we plot the absorption coefficient $\alpha$ for transmission values of $T_{peak}$ = 30% and 75% and filter widths of FWHM = 1 nm and 10 nm. The absorption in the reflectors is taken equal to zero, and the transmission band is assumed to be centered at $\lambda$ = 600 nm. For each transmission we allow several values for the free spectral range . The plots are of the absorption coefficient $\alpha$ versus the thickness of the etalon ($t = m\lambda/2n$ ). For all of these parameters, and assuming a reasonable film thickness of >50 nm, the maximum absorption in the EC material is on the order of $\alpha \sim 10\ \mu m^{-1}$.

# Potential Impact of Materials Optimization

The integration of EC materials into variable-index applications could potentially be expanded by varying the fundamental properties of the EC materials themselves. The optical constants of $WO_3$ can be changed by alloying, changing growth conditions, and by adding dopants. Several strategies are suggested in the literature. Miyake *et al.* were able to smoothly vary the optical band gap in $WO_3$ films between 2.7 eV and 3.25 eV by changing the substrate deposition temperature, thus altering the degree of crystallinity of the $WO_3$ films.[19] Ozkan *et al.* showed this same amorphous-to-crystalline phase transition altered the location of absorption bands in the 10- 12 μm range.[18] Tang *et al.* showed that the optical band gap of crystalline $WO_3$ could be varied between 2.8 and 1.9 eV by adding 1% of various metal cations such as $Mg^{2+}$, $Al^{3+}$, $In^{3+}$, $Fe^{3+}$, and $Zr^{4+}$.[20] Finally, Hiruta *et al.* showed that the location of the tunable absorption center in the VIS/NIR of amorphous thin films of $WO_3$ could be shifted up approximately 0.5 eV by alloying with $MoO_3$.[21]

This section leverages the derivation of the previous section, along with models of the optical constants of $WO_3$, to try to improve the performance of the modeled FP filter. As such we will focus on the optical constants of $WO_3$ at 600 nm.

Figure 37 shows the real (n) and complex (k) parts of the index of refraction for $WO_3$ at different intercalation levels. The curves are a fit of Lorentzian oscillators to the published data of von Rottkay *et al.* [22] While there are wavelengths where n varies widely with increasing intercalation, there are also wavelengths, such as at 1000 nm, where n doesn't vary at all. In addition to improving the performance of the filter at 600 nm, material optimization has the potential to allow the implementation of optical devices at wavelengths around 1000 nm.

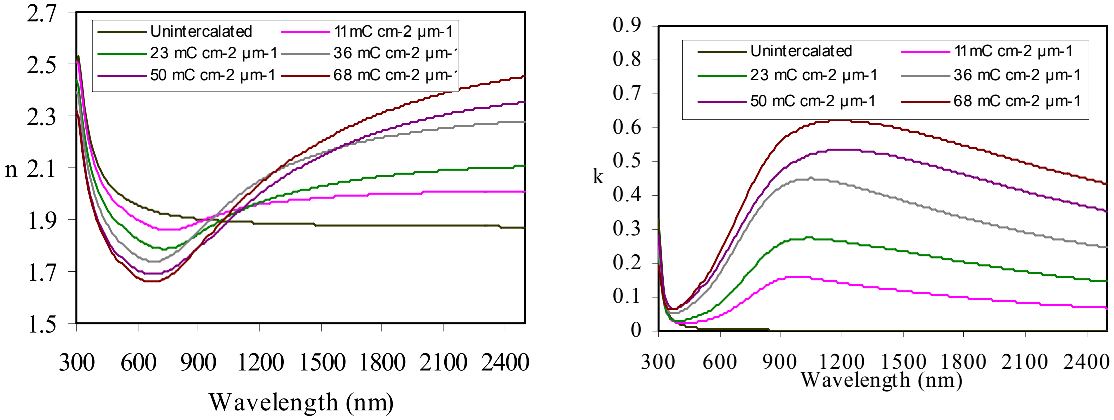

**Figs. 37 a and b: n and k of $WO_3$ vs. wavelength at different levels of intercalation (in mC/cm$^2$) after von Rottkay et al. [22]**

Figure 38 shows the potential for varying the material parameters of the $WO_3$. In the Lorentz oscillator (LO) model of the 11 mC cm$^{-2}$ μm$^{-1}$ $WO_3$, two LOs were required to model the absorption centers in the near-IR to visible range. According to Hiruta et al., the location of these centers in $WO_3$ can be shifted up approximately 0.5 eV if the $WO_3$ is alloyed with $MoO_3$.[21] In the LO models, the upper absorption center was located at 1.39 eV. Figure 38 shows this state of intercalation along with the unintercalated state. The two remaining curves show the effect of moving the absorption centers to +/- 0.5 eV of their nominal value.[*]

---

[*] This same approach could be taken with the other absorption centers in $WO_3$ (at the bandgap and the far IR W-O bond stretching absorption center). An initial screening study found that movement of this absorption center (1.39 eV) proved most effective at changing the n, k tradeoffs at the wavelengths (e.g. 600 nm) considered in this study.

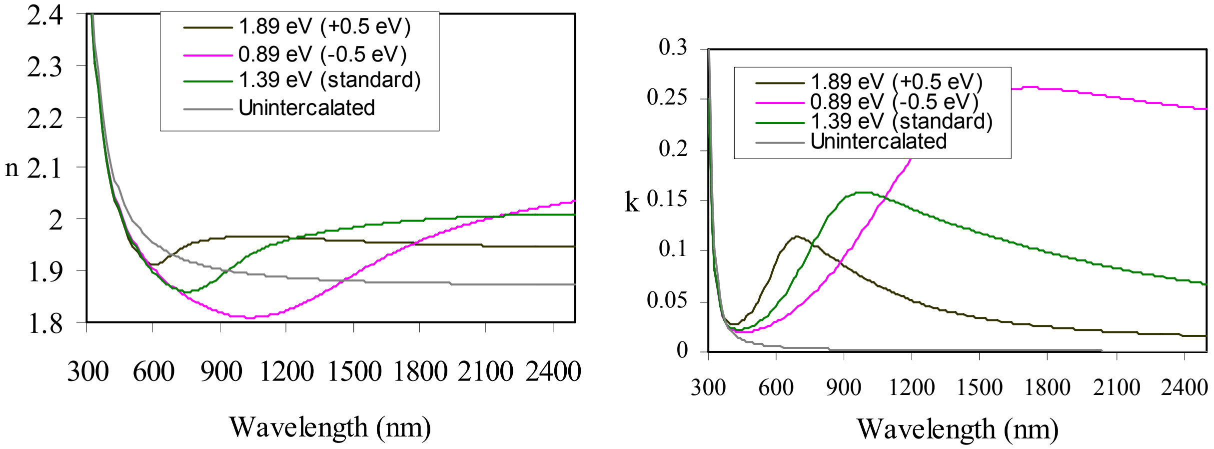

**Figs. 38 a and b n & k vs. wavelength for different absorption center locations. In addition to the nominal unintercalated and 11 mC cm$^{-2}$ µm$^{-1}$ intercalated (labeled 1.39 eV) curves are shown the +/-0.5 eV absorption center-adjusted curves**

Figure 39 shows the effect of adjusting the absorption centers for the remaining intercalation levels. The figure shows n vs. k at 600 nm for various levels of intercalation and movement of the absorption centers. The black dots are the original n and k values (taken from figure 37); the green and purple dots are the result of moving the absorption centers up by 0.25 eV and 0.5 eV, respectively; the red and blue dots are the result of moving the absorption centers down by 0.25 eV and 0.5 eV, respectively. The lines are best fits to the dots, assuming n = 1.95 when k = 0.

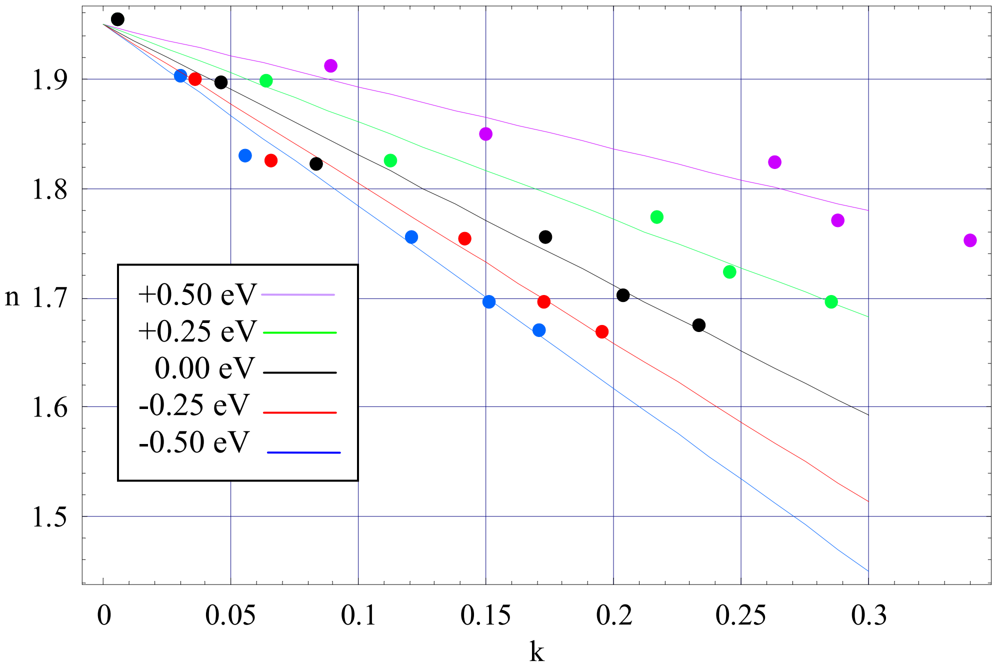

**Fig. 39 n vs. k for $WO_3$ at different levels of intercalation for different locations of the absorption center. Wavelength is fixed at 600 nm.**

Figure 40 integrates the analysis of the previous section with the current models. Assuming an FP filter whose only components are $WO_3$ and the reflectors, we calculated the maximum k for a given n for two sets of parameters. For both FP filters it was assumed λ=600 nm and n=1.95 (for the unintercalated case), A=0 and T=0.3. In the first FP filter the linewidth was fixed at 1 nm with a free spectral range of 10 nm. These requirements resulted in a film ~9.2 μm thick. The near-vertical line near k=.0007 are the calculated maximum absorptions for the various indices of refraction that keep within the above specified parameters. The other near-vertical line near k=.0065 is for an FP filter with a 10 nm linewidth and a free spectral range of 30 nm (resulting in a film thickness of ~0.31 μm).

Figure 41 shows the maximum possible change in index of refraction vs. absorption-center energy assuming the same conditions in Figure 39. The upper line represents the 1 nm-linewidth case, and the lower line the 10 nm-linewidth case. The black dots come from the unchanged case (Fig. 37). It is evident that the variability of the 1 nm-linewidth case cannot be improved substantially by moving the absorption centers. However, there is some improvement with the 10 nm-linewidth case. When one considers that the $WO_3$ is only a

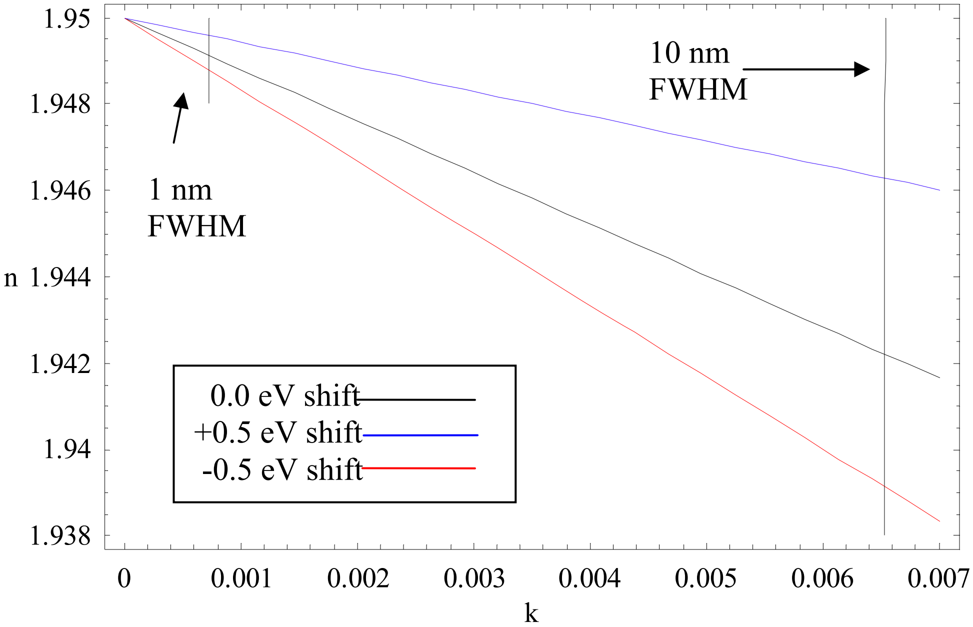

**Fig. 40 n vs. k lines for different absorption center locations and curves marking the maximum k for a given n.** See the text for details

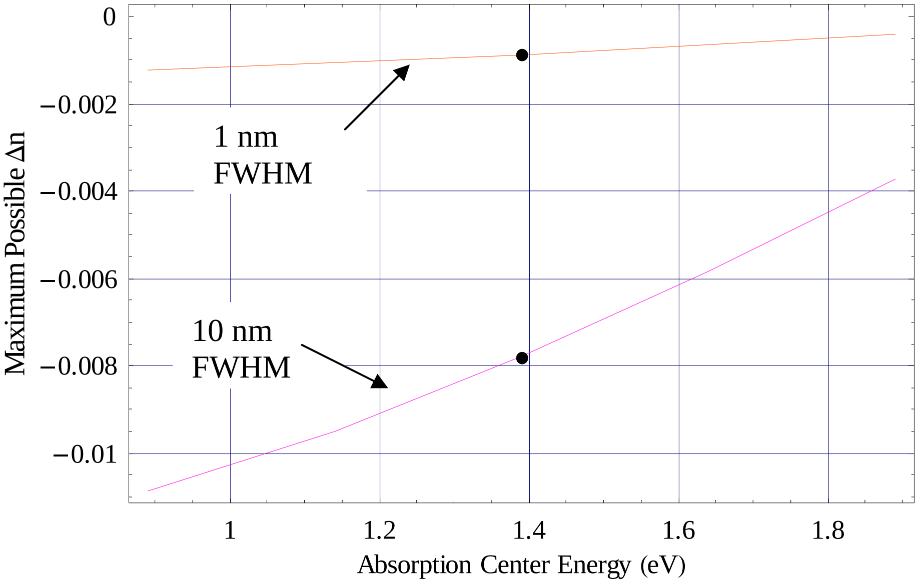

**Fig. 41 Maximum possible change in n vs. absorption center energy.**

fraction of the thickness of the optical cavity in a real EC-FP, like those fabricated in this study, it's clear that the maximum amount of tuning possible will be a fraction of the FWHM (although it appears that this fraction is bigger in a 10 nm FWHM filter than at 1 nm FWHM filter). However, the absorption penalties would not be as harsh. A more representative theoretical model may yield more accurate numbers; but the models can only go so far compared to experimental materials investigation. Additionally, careful consideration of Figs. 37 and 38 indicates that the tradeoffs determined in this analysis may be better at another wavelength. Furthermore a different EC material system than the one considered in this study might also have superior tradeoffs.

# Predicted filter performance of experimental stack

To supplement the data in Fig. 32, FP filter performance as a function of intercalation was modeled using the Film Wizard® software. Figure 42 shows the transmission of the filter as a function of intercalation using the models derived above from von Rottkay *et al.* [22] The black line is unintercalated $WO_3$ (optical constants measured from the $WO_3$ grown for this study), and the remaining curves are the fraction of intercalation to the 11 mC $cm^{-2}$ $\mu m^{-1}$ case, which is designated "1". The fraction of intercalation was created by multiplying the amplitude of the absorption center Lorentz oscillators by the corresponding decimal.

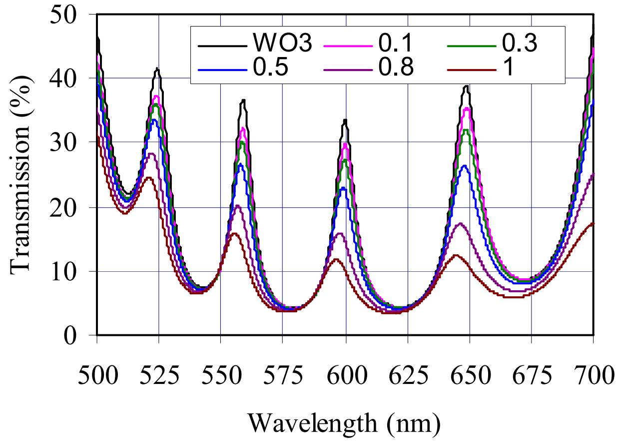

| | |
|---|---|
| 76.25 nm | Si3N4 |
| 101.6 nm | SiO2 |
| 76.25 nm | Si3N4 |
| 101.6 nm | SiO2 |
| 76.25 nm | Si3N4 |
| 101.6 nm | SiO2 |
| 320 nm | ITO |
| 435 nm | Rottky 11 WO3 |
| 300 nm | Ta2O5 |
| 30 nm | NiOH |
| 320 nm | ITO |
| 101.6 nm | SiO2 |
| 76.25 nm | Si3N4 |
| 101.6 nm | SiO2 |
| 76.25 nm | Si3N4 |
| 101.6 nm | SiO2 |
| 76.25 nm | Si3N4 |
| 1 mm | Generic SiO2 |

**Fig. 42 Transmission vs. wavelength modeled data. $WO_3$ designates the film grown for this study; the remaining curves are the fractions of intercalation to 11 mC $cm^{-2}$ $\mu m^{-1}$.** The modeled film stack is shown to the right of the graph.

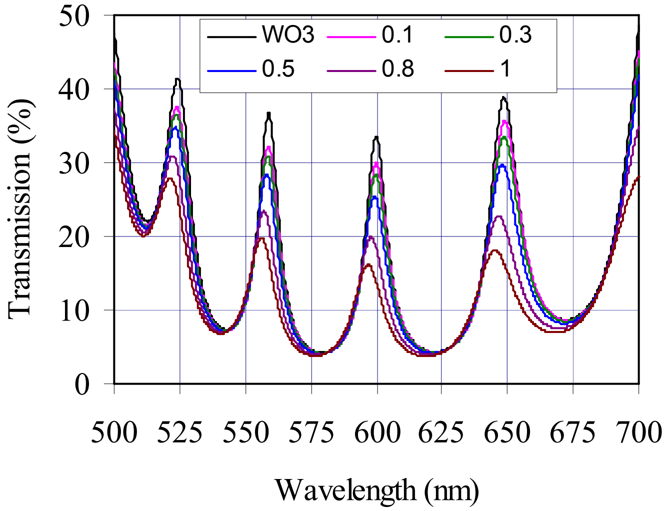

| | |
|---|---|
| 76.25 nm | Si3N4 |
| 101.6 nm | SiO2 |
| 76.25 nm | Si3N4 |
| 101.6 nm | SiO2 |
| 76.25 nm | Si3N4 |
| 101.6 nm | SiO2 |
| 320 nm | ITO |
| 435 nm | Rottky 11 WO3 |
| 300 nm | Ta2O5 |
| 30 nm | NiOH |
| 320 nm | ITO |
| 101.6 nm | SiO2 |
| 76.25 nm | Si3N4 |
| 101.6 nm | SiO2 |
| 76.25 nm | Si3N4 |
| 101.6 nm | SiO2 |
| 76.25 nm | Si3N4 |
| 1 mm | Generic SiO2 |

**Fig. 43 Same as Fig. 42, but with the absorption centers shifted down by 0.5 eV.** The modeled film stack is shown to the right of the graph.

Figure 43 shows the same modeled data as Figure 42, except that in figure 43 the absorption centers have been shifted down by 0.5 eV. It is evident that a similar peak shift is obtained with a slightly smaller amount of absorption. Careful reading of the data in Figs. 42 and 43 reveals that the unintercalated (labeled $WO_3$) peak is centered at 600 nm, has a transmission of 33%, and a FWHM of 9.6 nm (both Figs. 42 and 43). This can be tuned to 598 nm with a FWHM of 12.1 nm and a transmission of 16% (Fig. 42). If the EC $WO_3$ were optimized (Fig. 43), then a shift from 600 nm to 598 nm could be made with a FWHM of 11.3 nm and a transmission of 20%.

# Extension to SLMS

Another potential application of the electrically tunable refractive index in EC $WO_3$ is a spatial light modulator (SLM) used for phase correction (i.e. a wavefront corrector). An array of individually addressable EC phase shifting pixels might provide a means of correcting phase without altering the polarization state of the incoming wavefront. The data in Figs. 38 and 39 can be used to estimate the tradeoffs between absorption and phase shifting. If one assumes a pixel is comprised of a 1 μm thick film of $WO_3$ that can be tuned (the other films in the EC stack are ignored) like that in Figs. 38 and 39, then the absorption loss ($I/I_o = \exp(-\alpha t)$)[*] can be calculated as a function of optical path difference (OPD = Δn*thickness). Fig. 44 shows the results of this calculation for $WO_3$ at both 600 nm and 1000 nm. The impact of moving the mid IR absorption center is also considered in Fig. 44.

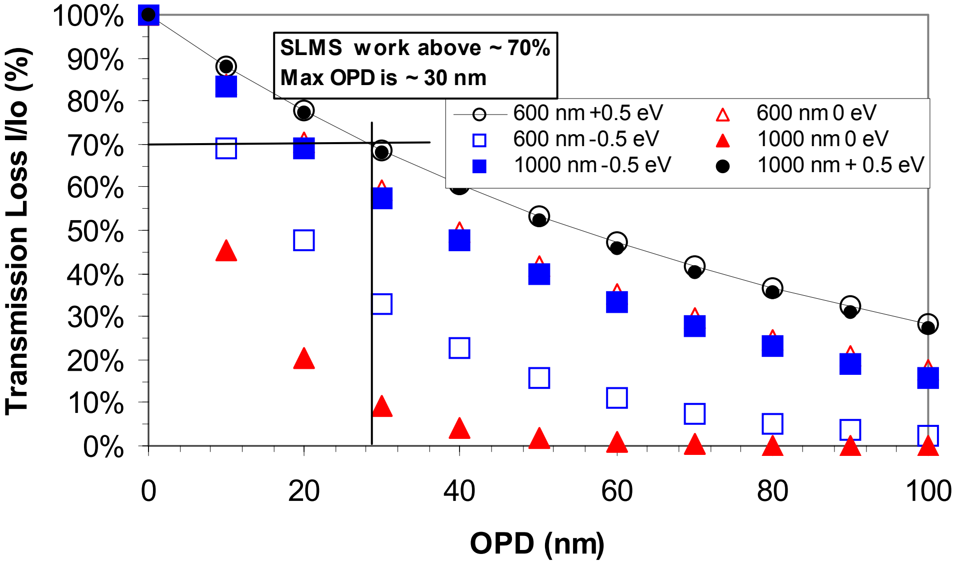

**Fig. 44 Illustration of tradeoff between phase shift and absorption penalty for wavefront correction with EC $WO_3$.** The transmission loss is plotted as a function of optical path difference (OPD) for a 1 μm $WO_3$ tunable dielectric material. Both 600 and 1000 nm wavelengths are considered, as is the impact of tuning the mid IR absorption center.

If one assumes that 70% transmission is required then the max OPD for any of the wavelengths and absorption center locations considered is 30 nm. The additional absorption in the $NiO_xH_y$ layer would tend to make this transmission even lower. Given this result, it would appear that transmission losses associated with phase shifting in EC $WO_3$ are too severe to be practical in phase shifting SLMS. We note, however, that other EC materials may offer a tradeoff of phase shift and absorption that is superior to that in $WO_3$. To our knowledge, no systematic investigation of EC materials has been conducted to address this problem.

---

[*] $\alpha = 4\pi k/\lambda$

# SUMMARY AND CONCLUSIONS

A combined experimental and modeling approach was used to evaluate the feasibility and benefit of incorporating an EC material stack with a tunable refractive index into an FP filter. The knowledge gained in this process was extended to speculate about the potential benefit of incorporating EC materials in SLMS as well.

The experimental effort was geared towards making an EC-FP film stack that had minimal absorption in the reflectors and did not require ambient humidity to operate like the first EC-FP prototype (produced during seed work for this project) that consisted of TiAu/$WO_3$/$Ta_2O_5$/Au. These changes help reduce absorption loss and narrow the FWHM. The stack in this study was $(Si_3N_4/SiO_2)_3$/ITO/$NiO_xH_y$/$Ta_2O_5$/$WO_3$/ITO/$(SiO_2/Si_3N_4)_3$.

Processes were developed to produce the individual component layers in the EC-FP filter. The optical and structural properties of these layers were characterized and a process flow to integrate these layers into working devices was developed. While numerous hurdles were overcome to successfully integrate the films into a working device, determining how to process the $NiO_xH_y$ charge storage layer proved to be the most difficult. Initially, elemental Ni was evaporated onto an ITO back electrode, which was used to vary the potential in a controlled pH environment in order to produce the appropriate oxide/hydroxide. Although this method produced a film that could be toggled between light and dark $NiO_xH_y$, it was severely cracked and partially peeled. This lead to shorting between front and back electrodes. Depositing a $NiO_x$ film via reactive sputtering onto an ITO back electrode and then treating it electrochemically to produce the proper $NiO_xH_y$ film yielded a much smoother film that was successfully incorporated into a working EC stack just before the conclusion of this project. Prior to resolving the process issues with the $NiO_xH_y$ film, a complete EC-FP filter stack was fabricated which had a peak transmission of 36% at 500 nm and a FWHM of 10 nm. This was dramatic improvement over the simple filter produced in the seed research project. While time ran out to incorporate the working EC stack into a full EC-FP filter, the optical data collected during the experimental effort was incorporated into the modeling effort, which predicted the performance.

Modeling was used to estimate the performance of the experimental EC-FP filter based on experimental and literature data and determine how alloying or doping $WO_3$ might be used to modify the n, k relationship in order to improve the performance of the experimental EC-FP filter. A general approach that takes into account the desired pass band location, pass band width, required transmission and EC optical constants in order to estimate the maximum tuning from any EC-FP filter was also developed.

Calculations indicate that minor thickness changes in the prototype stack developed in this project should yield a filter with a transmission at 600 nm of 33% and a FWHM of 9.6 nm, which could be tuned to 598 nm with a FWHM of 12.1 nm and a transmission of 16%. Additional modeling was performed to determine the potential impact of optimizing the $WO_3$ on this experimental EC-FP filter's performance. We estimate that optimizing the $WO_3$ would allow the same shift from 600 nm to 598 nm with a FWHM of 11.3 nm and a transmission of 20%.

In the general modeling approach, both 1 nm and 10 nm FWHM filters centered at 600 nm with 30% transmission were considered. While it appears that the materials optimization will improve the maximum amount of tuning possible more in the 10 nm FWHM filter, the maximum change in n still translates into a maximum level of tuning that is only a fraction (perhaps 20% from Fig. 42 and 43) of the FWHM in both cases. It's entirely possible however that other EC material systems may not have absorption problems this severe. Furthermore, the tradeoffs are different at other wavelengths (see Figs. 37 and 38). Therefore it is not inconceivable that an EC-FP filter could be constructed that self-corrects for temperature drift. Since temperature drift produces changes in the filter optical thickness that are 10-100 x smaller than one might expect from process uniformity problems (see introduction), correcting for process uniformity problems (thickness variation across a large area) using this approach will be significantly more difficult.

Finally, the results of materials optimization modeling were used to assess whether EC wavefront correction was possible. A simple calculation suggests that a maximum of 30 nm of OPD could be achieved before the transmission through a simple $WO_3$ pixel fell below 70%. Absorption in the other layers of the EC stack would only make the tradeoff worse. We therefore conclude the transmission losses are too large for this approach to be practical. However, we note that other EC material systems may have less severe absorption problems which could make this approach attractive.

# REFERENCES

[1] A. Yariv, *Optical Electronics* (Saunders College Publishing, Philadelphia, 1991).

[2] W. D. Kingery, H. K. Bowen, and D. R. Uhlmann, *Introduction to Ceramics*, 2nd ed. (John Wiley & Sons, New York, 1976).

[3] J. Matsuoka, N. Kitamura, S. Fujinaga, T. Kitaoka, and H. Yamashita, Journal of Non-Crystalline Solids **135,** 86-89 (1991).

[4] S. K. Deb, Philos. Mag. **27,** 801-822 (1973).

[5] F. G. K. Baucke, Materials Science and Engineering B **10,** 285-292 (1991).

[6] J. S. Hale, M. DeVries, B. Dworak, and J. A. Woollam, Thin Solid Films **313-314,** 205-209 (1998).

[7] G. Burns, *Solid State Physics*, 1st ed. (Academic Press, San Diego, 1985).

[8] D. R. Kammler, W. G. Yelton, W. C. Sweatt, and J. C. Verley, in *Use of Electrochromic Materials in Adaptive Optics*, San Diego, CA, 2005 (SPIE), p. 58950S-1 - 58950S-9.

[9] S. Deb (National Renewable Energy Lab), Personal Communication (2006).

[10] M. Pourbaix, *Atlas of Electrochemical Equilibrium in Aqueous Solutions* (NACE International Cebelcor).

[11] Jade®software (Materials Data Inc., Livermore, CA, 2002).

[12] G. Frank and H. Kostlin, Appl. Phys. A. **27,** 197-206 (1982).

[13] J.-H. Hwang, D. D. Edwards, D. R. Kammler, and T. O. Mason, Solid State Ionics **129,** 135-144 (2000).

[14] R. A. Synowicki, Thin Solid Films **313-314,** 394-397 (1998).

[15] J. A. Woollam, W. A. McGahan, and B. Johs, Thin Solid Films **241,** 44-46 (1994).

[16] N. Nadaud, N. Lequeux, M. Nanot, J. Jove, and T. Roisnel, Journal of Solid State Chemistry **135,** 140-148 (1998).

[17] C. G. Granqvist, Solar Energy Materials & Solar Cells **60,** 201-262 (2000).

[18] E. Ozkan, S.-H. Lee, C. E. Tracy, J. R. Pitts, and S. Deb, Solar Energy Materials & Solar Cells **79,** 439-448 (2003).

[19] K. Miyake, H. Kaneko, M. Sano, and N. Suedomi, J. Appl. Phys. **55,** 2747-2753 (1984).

[20] J. Tang, D. Wang, Z. Zou, and J. Ye, Materials Science Forum **423-425,** 163-166 (2003).

[21] Y. Hiruta, M. Kitao, and S. Yamada, Jpn. J. Appl. Phys. **23,** 1624-1627 (1984).

[22] K. v. Rottkay, M. Rubin, and S.-J. Wen, Thin Solid Films **306,** 10-16 (1997).

# Distribution

| | | |
|---|---|---|
| 1 | MS0734 | A. Ambrosini, 6215 |
| 1 | MS0867 | M. O. Eatough, 2725 |
| 1 | MS0867 | D. R. Kammler, 2725 |
| 1 | MS0964 | B. C. Brock, 5731 |
| 1 | MS0964 | J. A. Ruffner, 5731 |
| 1 | MS0980 | S. M. Gentry, 5703 |
| 1 | MS1082 | J. D. Blaich, 1723 |
| 1 | MS1082 | E. J. Heller, 1723 |
| 1 | MS1082 | J. J. Hudgens, 1725 |
| 1 | MS1082 | F. B. McCormick, 1727 |
| 1 | MS1082 | J. C. Verley, 1725 |
| 1 | MS1082 | W. C. Sweatt 1727 |
| 1 | MS1139 | M. T. Valley, 1535 |
| 1 | MS1425 | W. G. Yelton, 1725 |
| 2 | MS9018 | Central Technical Files, 8944 |
| 2 | MS0899 | Technical Library, 4536 |